Biomaterials 296 (2023) 122079

Contents lists available at ScienceDirect

Biomaterials

journal homepage: www.elsevier.com/locate/biomaterials

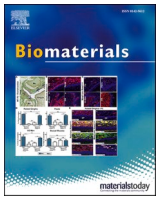

All-natural-molecule, bioluminescent photodynamic therapy results in complete tumor regression and prevents metastasis

Hao Yan, Sarah Forward, Kwon-Hyeon Kim, Yue Wu, Jie Hui, Anokhi Kashiparekh, Seok-Hyun Yun *

Harvard Medical School and Wellman Center for Photomedicine, Massachusetts General Hospital, 65 Landsdowne St., UP-5, Cambridge, MA, 02139, USA

ARTICLE INFO

Keywords:
Photomedicine
Bioluminescence
Breast cancer
Phototherapy
Biophotonics

ABSTRACT

Self-luminescent photodynamic therapy (PDT) has gained attention owing to its potential to enable effective phototherapy without the bottleneck of shallow light penetration into tissues. However, the biosafety concerns and low cytotoxic effect of self-luminescent reagents *in vivo* have been problems. Here, we demonstrate efficacious bioluminescence (BL)-PDT by using bioluminescence resonance energy transfer (BRET) conjugates of a clinically approved photosensitizer, Chlorin e6, and a luciferase, *Renilla reniformis*; both derived from biocompatible, natural molecules. With over 80% biophoton utilization efficiency and membrane-fusion liposome-assisted intracellular delivery, these conjugates produce effective, targeted cancer cell killing. Specifically, in an orthotopic mouse model of 4T1 triple-negative breast cancer, BL-PDT showed strong therapeutic effects on large primary tumors and a neoadjuvant outcome in invasive tumors. Furthermore, BL-PDT resulted in complete tumor remission and prevention of metastasis for early-stage tumors. Our results demonstrate the promise of molecularly-activated, clinically viable, depth-unlimited phototherapy.

1. Introduction

Photodynamic therapy (PDT) is a therapeutic treatment modality for many diseases, including cancers [1,2]. PDT employs light and photosensitizers that, upon absorbing photon energy, generate reactive oxygen species (ROS) that can lead to various therapeutic effects, such as killing malignant cells and activating anti-tumor immune responses. However, effective PDT critically relies on a sufficient light dose at target tissues, typically requiring an optical fluence of ~50 J cm^{-2} at the surface of the tissue. This dose can produce PDT effects at tissue depths up to a few millimeters below the surface [3–7]. This shallow depth has confined PDT to superficial structures and requires extrinsic, fiber-optic light sources to treat endoscope-accessible tissues [8].

To overcome these limited therapeutic depths, a promising strategy for replacing the external light illumination of conventional PDT is by use of self-luminescence based on chemiluminescence (CL) [9–12] or bioluminescence (BL) as an internal light source [13–17]. Although molecular luminescence has a much weaker intensity than conventional light sources, such as lasers and light-emitting diodes, efficient Förster resonance energy transfer (FRET) from the luminescent group to photosensitizers can, in principle, compensate for the difference in intensity and produce substantial PDT effects. Recently, several combinations of self-luminescent donors (CL or BL) and photosensitizer acceptors have been reported, showing ROS-induced cell death *in vitro* and appreciable tumor growth inhibition *in vivo* [9,10,16,17]. However, current self-luminescent PDT is confronted with two major problems: First, the *in vivo* therapeutic efficiency is modest. This is mainly limited by low luminous efficiency (quantum yields <0.1 [18]) for the case of chemiluminescence-PDT (CL-PDT) [9,10], which relies on endogenous H_2O_2 at low concentrations, and the low capture and utilization rate (<40%) of biophotons in the case of bioluminescence-PDT (BL-PDT) [15–17]. Second, the self-luminescent reagents demonstrated so far present cytotoxicity concerns: luminol used in CL-PDT has a high affinity to serum albumin and DNA, raising concerns about biosafety [14,19]. Quantum dots used in BL-PDT also bring with them the risk of inorganic nano-material toxicity [13–15].

Here, we report highly efficient bioluminescence resonance energy transfer (BRET)-induced BL-PDT enabled by a novel reagent consisting of a clinically used photosensitizer, Chlorin e6 (Ce6), and the *Renilla reniformis* Luciferase 8 (RLuc8) protein. As both Ce6 and RLuc8 are natural or naturally derived molecules, RLuc8-Ce6 conjugates offer promising potential for clinical translation. Optimized RLuc8-Ce6

* Corresponding author.
E-mail address: syun@hms.harvard.edu (S.-H. Yun).

https://doi.org/10.1016/j.biomaterials.2023.122079
Received 9 November 2022; Received in revised form 27 February 2023; Accepted 2 March 2023
Available online 2 March 2023

conjugates achieve 80% activation efficiency (i.e., the probability of producing one activated Ce6 molecule per BL photon) and are efficiently transported into cancer cells via fusogenic nano-liposomes. We compare the effects of BL-PDT with conventional PDT for 4T1 murine and MDA-MB-231 human triple-negative breast cancer (TNBC) cells *in vitro* and then in *in vivo* orthotopic mouse models. Our results show strong therapeutic BL-PDT effects on larger tumors (7–8 mm) as well as neo-adjuvant effects at tumor margins. We also demonstrate complete tumor remission and metastasis prevention in the sentinel lymph nodes and lungs.

2. Materials and methods

2.1. Synthesis of Luc-Ce6 conjugate

The Luc-Ce6 conjugate was synthesized by directly conjugating Renilla luciferase 8 (Rluc8, or simply Luc, G-Biosciences) with chlorin e6 mono 6-amino hexanoic acid amide (Ce6-HA) molecules (Santa Cruz Biotechnology) using the standard N-(3-dimethyl aminopropyl)-N-ethyl-carbodiimide hydrochloride (EDC)/N-hydroxysulfosuccinimide (Sulfo–NHS)–activated condensation reaction. Briefly, 1 mg Ce6-HA (1.4×10^{-6} mol) powder was thoroughly dispersed in 100 μl dimethyl sulfoxide (DMSO) and then mixed with 400 μl DPBS buffer to make a 0.5 ml, 2 mg ml^{-1} solution. Then, 100 μl E.D.C. (2.6×10^{-5} mol) and 50 μl Sulfo-NHS (4.6×10^{-6} mol) were added into a Ce6-HA solution and reacted for 20 min at room temperature. After this crosslinking reaction, 447 μl 2-mercaptoethanol (55 mM) was added to the solution to quench the excess EDC, and the sample was incubated for 10 min at room temperature. For conjugation, a new modified Ce6-HA solution was added into a Rluc8-DPBS solution, gently pipetted several times, and then reacted for 3 h in an Eppendorf ThermoMixer-C instrument (300 rpm) at room temperature. The ratio of Ce6-HA and Rluc8 was varied to test different mole conjugation ratios. After conjugation, the mixture solution was filtered using Zeba spin desalting columns (7K MWCO) to eliminate unreacted small molecules and obtain the final Luc-Ce6 DPBS solution.

2.2. Characterization of Luc-Ce6 conjugate

An electron-multiplication charge-coupled device (EMCCD)-equipped spectrometer (Newton, Andor) was used to measure bioluminescence (BL) spectra from various solutions. To measure BL spectra from RLuc8 and methoxy e-coelenterazine (Me-eCTZ, or simply CTZ), 1 ml, 0.3 μM CTZ was added to a 1 ml, 0.3 μM Luc-Ce6 DPBS solution in a polystyrene cuvette. The BL emission was collected with 0.1 s exposure and 300 frame averaging. The fluorescence spectra of Ce6-HA solutions (from 1.7 to 24.9 μM) and Luc-Ce6 solution (0.38 μM) were measured by using the EMCCD-coupled spectrometer and a xenon lamp filtered by a monochromator. A microplate reader (Epoch 2, Biotek Instruments) in the spectrophotometer mode was used to measure the absorption spectra of Ce6-HA at different concentrations (from 8.3 to 166 μM) and of Luc-Ce6 conjugates (1.39 and 2.78 μM). A dynamic light scattering instrument (Malvern Zetasizer Nano-ZS, 633 nm) was used to measure the hydrodynamic size and Zeta potential.

2.3. Detection of singlet oxygen in solution

A singlet oxygen sensor green dye (SOSG, Thermo Fisher Scientific), highly selective for $^1O_2$, was used to measure the amount of singlet oxygen in the solution. A mixture solution of Luc-Ce6 or Ce6-HA with SOSG (dissolved in methanol) was prepared (10 μM SOSG in the mixture), and CTZ with different molar ratios (20–150) was added to BL-PDT sample solutions. The laser-PDT sample solutions were illuminated with a 405 nm laser beam at 1 J cm^{-2}. The fluorescence spectra of the samples were measured 30 min after treatments.

2.4. Fusogenic nano-liposomes (Fuso-lip) and Luc-Ce6 loading

The two main components of liposomes, 1,2-dioleoyl-3-trimethylammonium-propane (DOTAP) and 1,2-dioleoyl-*sn*-glycerol-3-phosphoethanolamine (DOPE) were purchased from Avanti Polar Lipids (stored at −80 °C). A 1 mg ml^{-1} stock solution of DOPE/DOTAP with a weight ratio of 1:1 was prepared. After evaporating the chloroform solvent, DOPE and DOTAP were resuspended in DPBS buffer at 1 mg ml^{-1} concentration. For Luc-Ce6 loading, a 500 μl, 27.8 μM fresh solution of Luc-Ce6 was added into an 800 μl DOPE/DOTAP solution, stirred vigorously for 10 min (300 rpm), and incubated in an ultrasonic bath (Elmasonic, 37 kHz, 30% power) for 5 min at room temperature. To reduce the size of conjugate-loaded liposomes, a mini-extruder instrument (Avanti Polar Lipids) was used to gently extrude the Luc-Ce6/Fuso-lip solution several times through membrane filters with 100 nm pore sizes for *in vitro* experiments or 50 nm pore sizes for *in vivo* experiments. After extrusion, 3,3′-dihexadecyloxacarbo-cyanine perchlorate (DiO) or 1,1′-dioctadecyl-3,3,3′,3′-tetramethyl-lindotricarbocyanine iodide (DiR) was added into the liposome solution with a ratio of 1/15 (w/w) for fluorescent staining of the liposomes. The sample was diluted with DPBS buffer to the desired working concentration.

2.5. Cell culture and in vitro cytotoxicity evaluation

Murine fibroblast L929 cell line cells, murine TNBC 4T1 cells, and human TNBC MDA-MB-231 cells were purchased from ATCC (American Type Culture Collection). Cells were cultured in recommended standard conditions. DMEM basic cell media was supplemented with fetal bovine serum (10%, v/v) and penicillin/streptomycin (1%, v/v), known as "complete media." Cells were incubated at 37 °C in a humidified atmosphere of 5% CO_2 and 95% air. For the cytotoxicity studies, cells were seeded on a 96-well plate (~5000 cells per well) with 100 μl complete media and cultured for 24 h prior to adding different test reagents: CTZ (25, 50, and 100 μM), Fuso-lip (50, 75, 100, and 150 μg ml^{-1}), or Luc-Ce6/Fuso-lip (0.75, 1.25, 1.7, 2.5, 3.3, 5.0, 6.7, and 10 μM). After incubation for 4 h for CTZ and 30 min for Fuso-lip and Luc-Ce6/Fuso-lip, the cells were washed two times by DPBS buffer and cultured in fresh cell media for 24 or 48 h. The cell viability was measured by using a cell counting kit-8 (CCK-8, ApexBio) assay. The absorbance was measured by using a spectrophotometer (Epoch 2, Biotek Instruments).

2.6. Intracellular delivery of Luc-Ce6 conjugate

Cells were plated in glass-bottomed well plates with the same density. After culturing for 24 h, the cell media was removed, a Luc-Ce6/Fuso-lip DPBS solution was added, and the cells were incubated for 30 min. After removing the Luc-Ce6/Fuso-lip solution, the cells were washed three times and cultured in fresh cell media for further experiments or fixed by 4% paraformaldehyde (PFA) for imaging. As a control group, Ce6-HA solution was added to the culture plate and incubated for 2 h before fixing with 4% PFA. The cell nuclei were stained with 4′,6-diamidino-2-phenylindole (DAPI). A lyso-tracker probe (Invitrogen, Red DND-99) was used to stain intracellular lysosomes. 1 mM probe stock solution was diluted to 1 μM in DPBS buffer and added to the cells in glass-bottom plates to reach 50 nM in the media. After 1 h incubation, the cells were washed 3 times with DPBS buffer, fixed with 4% PFA, and examined with fluorescence confocal microscopy. A mitochondria tracker Red CMXRos dye (Invitrogen) and 2′,7′-dichlorodihydrofluorescein diacetate (DCFDA, Cell Biolabs) was used for mitochondrial and intracellular ROS staining, respectively. The Mito-Tracker probe was dissolved in DPBS buffer to prepare a 50 nM solution. DCFDA was dissolved in DMSO to form a stock solution (of 500 μM) and diluted into the Mito-Tracker DPBS buffer to obtain a 5 μM working solution. After incubation with Luc-Ce6/Fuso-lip, 4T1 cells in a glass-bottom plate were washed twice with DPBS and added to the Mito-Tracker/DCFDA-DPBS mixture solution. After further incubation for 30 min at 37 C, the cells

were washed three times, fixed, and stained with DAPI for imaging.

2.7. Measurement of intracellular ROS

4T1 Cells were plated on a glass-bottomed plate. After cultured for 24 h, Luc-Ce6/Fuso-lip or Ce6 DPBS solution was added and incubated for 30 min or 2 h, respectively. After washing twice with DPBS, a 50 nM DCFDA/DPBS labeling solution was added into the cell culture and incubated for 30 min at 37 C. For the BL-PDT group, CTZ (100 μM) was added, and the cells were incubated for 4 h. For the laser-PDT group, a 405 nm laser was illuminated with a fluence of 1 J cm^{-2}. After completing the treatment, the cells were washed three times and fixed by 4% PFA for imaging.

2.8. Assessment of therapeutic effects in vitro

g with DPBS, the cells received Luc-Ce6/Fuso-lip at different concentrations and incubated for 1 h at 37 °C. Next, the cells were washed with DPBS, received 100 μM CTZ, and incubated for 4 h. The cells were then washed and rested for 24 h at 37 °C. The viability of the cells was measured by using the CCK-8 assay. Control cells underwent the same washing and incubation process without adding Luc-Ce6 and CTZ reagents. For laser-PDT, cells were incubated with a Ce6-HA DPBS solution for 2 h and then irradiated with a 405 nm laser for 1 J cm^{-2}. A Live/Dead™ cell imaging kit (Invitrogen) was used for imaging analysis of cell viability. 4T1 cells were incubated for 24 h, rinsed with DPBS, and stained with the live/dead kit for 15 min at room temperature. Finally, the cells were washed with DPBS and fixed by 4% PFA for imaging. For apoptosis assay, 4T1 cells were plated in 24-well plates at a density of 5 $\times$ 10^4 cells per well and cultured for 24 h. After incubation with Luc-Ce6/Fuso-lip for 30 min or Ce6 for 2 h, 4T1 cells were treated with 100 μM CTZ for BL-PDT and 405 nm laser (1 J cm^{-2}) for laser-PDT. After incubation for 24 h, the cells were harvested, washed twice with cold DPBS, and then resuspended in DPBS buffer. The cell solution was then mixed and incubated with Annexin-V-FITC and PI (Abcam) working solution for 20 min at room temperature. Flow cytometry (BD FACSAria Cell Sorting System) was used to measure the apoptosis signals from the fluorescent probes.

2.9. Tissue penetration efficiency study in vitro

To measure the penetration depth of the 405 nm laser, chicken breast tissue slices with a thickness of 50 μm each were prepared through standard freezing tissues and cryosection. Each breast tissue slice was fully spread and put on a glass slide. The glass slides were stacked on top of each other to simulate thicker tissues (50 μm for one slice to 300 μm for 6 stacks). 4T1 cells were prepared in a plate and incubated with Ce6-HA for 2 h. Then, 405 nm laser light with a fluence 1 J cm^{-2} was illuminated on top of the first tissue slice. The optical attenuation through tissue stacks was measured using an optical power meter (Thorlabs, PM400). After the laser-PDT, the cells were incubated for 24 h, and their viability was measured using the CCK-8 assay.

2.10. In vivo tumor model

According to the NIH guidelines, all animal studies and related protocols (2015N000205) have been reviewed and approved by the MGH Institutional Animal Care and Use Committee (IACUC). BALB/c female mice (5–6 weeks old) were purchased from Jackson Laboratories. A metastatic TNBC orthotopic model was produced by carefully injecting ~10^6 4T1 tumor cells into the mammary fat pad of a mouse. The tumor volume was measured from Week 1 following inoculation by external manual examination. The tumor volume was calculated as (length times widthˆ2) 2^{-1}. Each week post-inoculation, tumor tissues, sentinel Lymph nodes (SLNs), and lungs were harvested to analyze the extent of tumor invasion and metastasis. Tissue sections were stained with Hematoxylin & Eosin (H&E) and antibodies against Ki-67 and epidermal growth factor receptor (EGFR).

2.11. In vivo biodistribution after intratumoral delivery

Ce6/Fuso-lip PBS solution was injected into the tumor at several locations to cover the entire volume of the tumor at a 2.5 mg kg^{-1} dose (based on the Luc-Ce6 amount). Mice were sacrificed at 6 h after injection. The entire tumor was carefully collected and quickly frozen in OCT gel (Tissue-Tek®) for cryosection. To obtain the spatial distribution of Luc-Ce6 in the tumor, four tumor slices (8 μm thick each) were cut with an inter-slice distance of 50 μm. The sham-treated control group received the same multipoint intratumoral injection of PBS. The tumor slices were imaged using a fluorescence microscope (Keyence, BZ-X700).

2.12. In vivo antitumor efficacy

For initial assessment, 4T1 tumor-bearing mice were randomly divided into 4 groups (n = 3 each), each receiving PBS, Luc-Ce6/Fuso-lip only, BL-PDT, and laser-PDT. On Day 14, after tumor inoculation, Luc-Ce6/Fuso-lip PBS solution was directly injected into the tumor at multiple locations at 2.5 mg kg^{-1} dose. 50 μl PBS was injected into the PBS group. For the BL-PDT group, 50 μl CTZ (100 μM) was intravenously injected into the tail vein at 6 h after the injection of Luc-Ce6/Fuso-lip, and additional CTZ with the same amount was administered every 4 h for a total 20 h duration. For the laser-PDT group, the skin directly on top of the tumor was irradiated with a 405 nm laser with a dose of 90 J cm^{-2}3 days after treatment, the mice were euthanized, and the whole tumors were collected and fixed in 4% PFA for 2 days. Then the tumor tissues were transferred for staining for H&E, Ki-67, EGFR, and TUNEL following the standard protocol. The tissue slices were scanned by using a Nanozoomer Slide Scanner (Hamamatsu).

For testing early-stage tumor treatments, mice with orthotopic 4T1 tumors were randomly divided into 4 groups (n = 5 each). On day 7, after tumor inoculation, Luc-Ce6/Fuso-lip PBS solution was injected into the tumor in 2.5 mg kg^{-1} dose. Starting from 6 h after the injection, CTZ (100 μM) was intravenously injected into the BL-PDT group 6 times with an interval of 4 h. In addition, a single 405 nm laser irradiation (90 J cm^{-2} at the skin) was given to the laser-PDT group. Following the treatments, the tumor size, body weight, and general health conditions of the mice were measured every other day. 17 days after the completion of the treatment, the mice were euthanized. Sentinel lymph nodes (SLNs) and lungs were collected and fixed with 4% PFA for 1 day and embedded into paraffin for sectioning. Tissue sections of the SLNs and lungs were stained with H&E and antibodies against Ki-67 and EGFR. Additionally, various other organs, such as the heart, liver, kidney, and spleen, were also harvested, fixed by 4% PFA, and examined by H&E histology.

2.13. BL-PDT for neoadjuvant therapy

2 weeks post tumor inoculation, mice with orthotopic 4T1 tumors were randomly divided into PBS control, Laser-PDT, and BL-PDT groups (n = 3 each). For the laser-PDT and BL-PDT groups, Luc-Ce6/Fuso-lip-PBS solution (1.0 mg kg^{-1}) was carefully injected into the tumor boundaries on all sides using a fine needle. For distribution measurement, 6 h after the injection, the tumor, and its neighboring normal tissues were harvested and quickly frozen in OCT gel for cryo-sectioning. For testing neoadjuvant therapy, 50 μl CTZ (100 μM) was intravenously injected every 4 h, a total of 6 times for the BL-PDT group. In addition, 90 J cm^{-2} of 405 nm laser was given to the laser-PDT group. 5 days after treatment, tissues, including the tumor boundary, were harvested and fixed in 4% PFA for staining for H&E, Ki-67, EGFR, and TUNEL.

2.14. Statistical analysis

The data are presented as means ± standard deviation, as noted in each case. The number of samples, n, is provided. A two-way analysis of variance (ANOVA) was used. $P < 0.05$ was considered to indicate a statistically significant difference. $P < 0.05$, $P < 0.01$, and $P < 0.001$ are indicated with single, double, and triple asterisks, respectively.

3. Results

3.1. Synthesis and BRET efficiency of Luc-Ce6 conjugate

Scheme 1a illustrates the working principle of the Luc-Ce6 conjugate. Briefly, Ce6-HA molecules (710 Da) were conjugated to RLuc8 proteins (~37 kDa) using EDC/Sulfo-NHS chemistry (Fig. S1). The conjugation was formed between the surface-active amino residues of Rluc8 protein (at least 39 from a total of 311 amino acid residues [20,21]) and the acid amide of the Ce6-HA, resulting in Ce6 conjugated on the surface of RLuc8. When a substrate methoxy e-coelenterazine (Me-eCTZ, or briefly CTZ hereinafter) binds with RLuc8 (briefly Luc8), the BL reaction produces energy that is desired to be transferred to one of the Ce6 molecules via BRET. In addition, the excited Ce6 may react with an oxygen molecule nearby and convert it to singlet oxygen ($^1O_2$). This probability of ROS generation from activated Ce6 is 65–70% in typical *in vitro* and *in vivo* conditions [22,23].

A mixture of Luc8 and CTZ in solution emits BL photons with a center at 415 nm, which overlaps well with the absorption peak of Ce6 at 406 nm (Fig. 1a). When Luc8 (0.3 μM) and Ce6-HA (7.5 μM) were simply mixed in solution with CTZ, fluorescence from Ce6 at 660 nm appeared (Fig. 1a) due to the absorption of BL photons by Ce6 and BRET from Luc8/CTZ to Ce6 molecules in proximity (<5 nm). We fabricated Luc-Ce6 conjugates with different ratios of Ce6 to Luc8. As the ratio increased from 15:1 to 42:1, the BL intensity at 440 nm decreased. The fluorescence intensity at 660 nm reached the maximum at a ratio of 25:1 (Fig. 1b S2b, and S3b). A simple kinetic model considering a BRET efficiency and hindrance of Ce6 to the interaction of Luc explained the experimental result reasonably well (Fig. 1c). We determined 25:1 to be the optimal ratio and used this value in all subsequent experiments.

Fig. 1d shows the representative emission spectrum of Luc-Ce6 conjugates (0.3 μM), integrated over 1 min (BL of Luc lasts about 1 min [15]), with CTZ (~1 μM). The BRET ratio, defined by the ratio of total acceptor emission (B, 600–800 nm) to the total donor emission (A, 400–600 nm), was 0.71. The ratio of activated Ce6 molecules (transferred photons) to the total number of produced BL photons was 80% (Table S1). This is a remarkably high efficiency of excitation. For far-field illumination, the absorption cross-section of Ce6 is $\sim 1 \times 10^{-15}$ cm^2 at 405 nm, which means 10^{15} photons in 1 cm^2 are needed to excite a single Ce6 molecule. In conventional PDT using far-field illumination, most photons are not absorbed by photosensitizers and are wasted. By contrast, 80% of BL photon is used to excite Ce6 (Table S1).

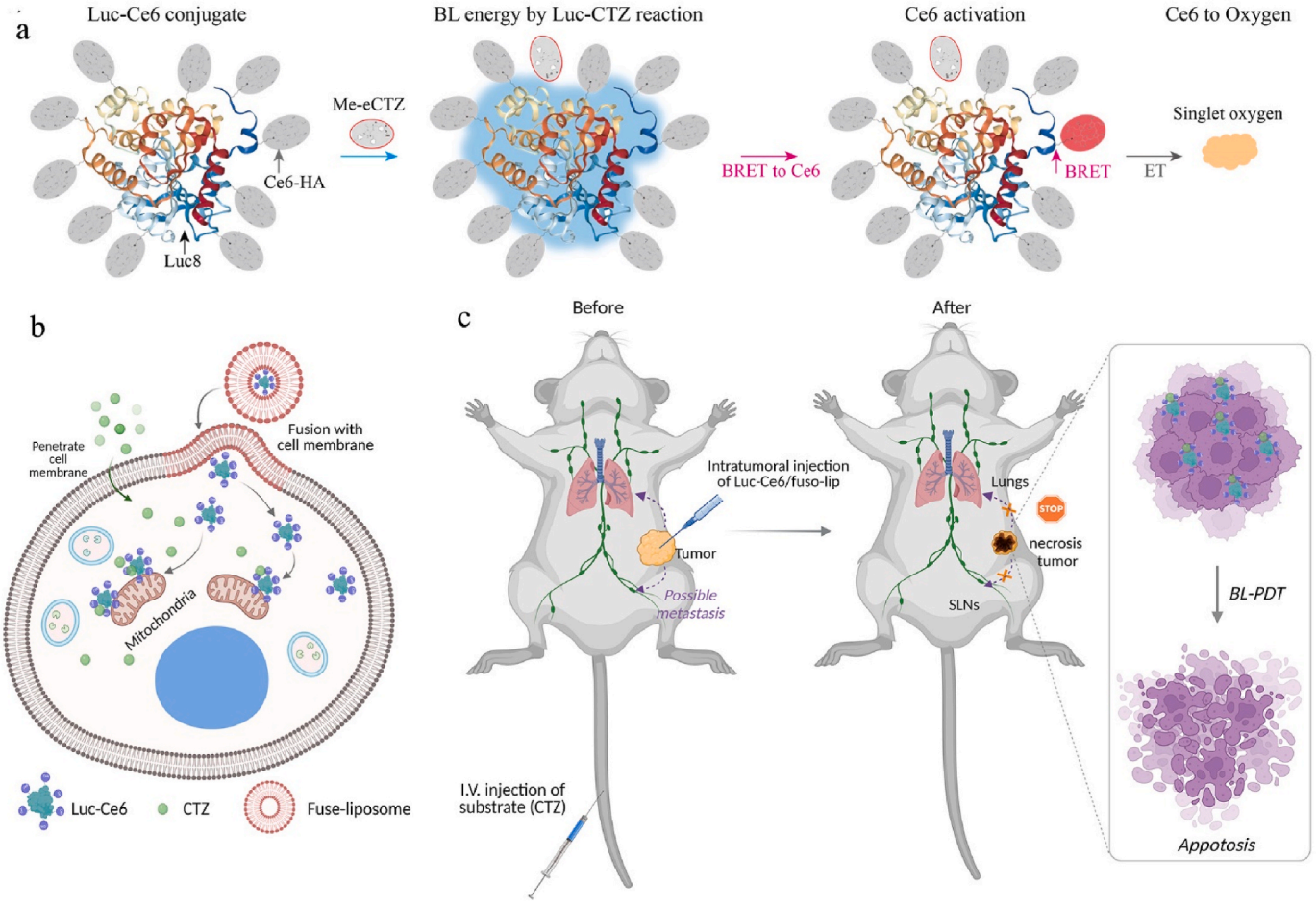

Scheme 1. BL-PDT on 4T1 triple-negative breast cancer tumors (TNBC) *in vivo*. (a) Schematic of the structure of Luc-Ce6 conjugate and its bioluminescence resonant energy transfer (BRET) principle. Upon administration of substrate Me-eCTZ, the generated bioluminescence resonant energy from the Luc8 core is transferred to the conjugated Ce6 molecule and subsequently activated Ce6 to produce therapeutic reactive oxygen species. (b) Schematic illustration of intracellular delivery of Luc-Ce6 by fusogenic nanoliposomes (Fuso-lip). (c) BL-PDT by locally injected Luc-Ce6 and systematically injected CTZ results in complete tumor remission and prevention of metastasis of TNBC tumors.

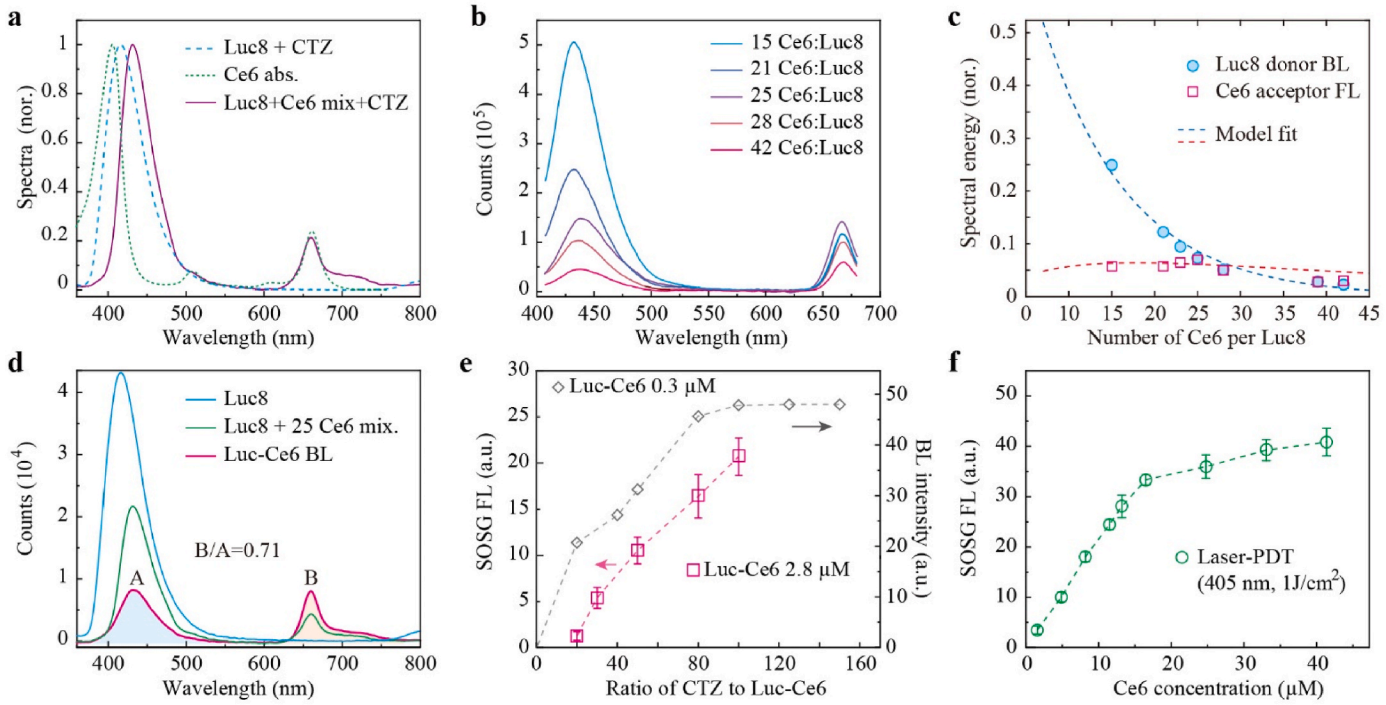

Fig. 1. Physicochemical characterization of the Luc-Ce6 conjugate. (a) Normalized BL spectrum of Luc (blue), absorption spectra of Ce6 (green), and BL spectra of the mixture of Luc and Ce6 (the ratio is 1:25) (purple). (b) BL spectra of Luc-Ce6 conjugates with different mole conjugation ratios of Ce6 molecules to Luc protein. (c) The dependence of spectral energy calculated from BL spectrums for the donor and acceptor on the number of Ce6 molecules per Luc8. (d) BL spectra of Luc8 protein (0.3 μM), the mixture of Luc (0.3 μM) and Ce6 (7.5 μM), and Luc-Ce6 conjugate (0.3 μM for Luc). A: donor emission (400–600 nm) area, B: acceptor emission (600–800 nm) area. (e) Changes in the BL and SOSG fluorescence intensity as the proportion of substrate CTZ varied at two different concentrations of Luc-Ce6. (f) SOSG fluorescence intensity as a function of Ce6 concentration in solution after laser-PDT. (For interpretation of the references to colour in this figure legend, the reader is referred to the Web version of this article.)

We used a singlet oxygen sensor green (SOSG) dye to detect $^1O_2$ generated by Luc-Ce6 and CTZ in solution [24]. The SOSG fluorescence intensity increased nearly linearly with increasing CTZ (Fig. 1e) before it saturated when the ratio of CTZ to Luc8 exceeded 100. A similar trend was observed with conventional laser-PDT using Ce6-HA as the photosensitizer and 405 nm laser irradiation (Fig. 1f and Fig. S5). Regarding singlet oxygen generation, 280 μM CTZ on 2.8 μM Luc-Ce6 is equivalent to laser fluence of 1 J cm^{-2} on 10 μM Ce6.

3.2. Intracellular delivery of Luc-Ce6 conjugates

Intracellular delivery of protein constructs has been challenging [25,26]. We found fusogenic nano-liposomes (Fuso-lip) to have a high affinity to the cell membrane (Fig. S6 and Fig. S7). Fuse-lip, upon fusing into the cellular membrane, can directly inject cargo into the cytoplasm (Scheme 1b) [27]. We loaded Luc-Ce6 conjugates in Fuso-lip using a charge differential drive followed by membrane extrusion through 50 nm pores. The final Luc-Ce6/Fuso-lip complex had a zeta potential of −17.8 mV (Fig. S8). We tested intracellular delivery with 4T1 murine breast cancer cells. We found fuso-lip to fuse immediately with the cell membrane and deliver Luc-Ce6 conjugates into the cytosol (Fig. 2a and S9). The cells incubated with 5 μM Luc-Ce6 (containing 75 μM Ce6) in Fuso-lip exhibited even stronger Ce6 fluorescence than cells incubated with 25 μM Ce6-HA for 120 min incubation time. Flow cytometry analysis supported the effectiveness of Luc-Ce6 delivery by Fuso-lip, which was comparable to the intracellular uptake of small Ce6-HA molecules (Fig. 2b). The intracellular distribution of Luc-Ce6 was not correlated with the distribution of lysosomes (Fig. 2c, S10, and S11). This supports that the uptake mechanism of Luc-Ce6/Fuso-lip escapes from typical endocytosis and does not involve the endosomal-lysosomal system [28]. Ce6 molecules accumulate in the mitochondria membrane after entering cells partly because of their hydrophobic aromatic rings [29]. This association with mitochondria is important for the cytotoxicity of PDT [30]. We observed an overlap of mitochondria with Ce6 and Luc-Ce6 (Fig. 2d, S12, and S13), as well as the fluorescence from DCFDA, an intracellular ROS sensor, in both laser-PDT (Fig. S14) and BL-PDT (Fig. S15). Given the similar intracellular distributions, we expect the cytotoxic mechanism to be similar between BL-PDT and laser-PDT using Ce6.

We further assessed the delivery and distribution of tumors after intratumoral injection of Luc-Ce6/Fuso-lip. The hydrodynamic size of the Luc-Ce6/Fuso-lip complex was about 100 nm (Fig. 2e). Luc-Ce6/Fuso-lip (2.5 mg kg^{-1}) was intratumorally injected into the TNBC orthotopic tumor (~180 mm^3) using a fine needle at several sites. In addition, we harvested tumors 6 h after intratumoral injection of Luc-Ce6/Fuso-lip and found the reagent distributed extensively in the tumor (Fig. 2f, S16, and S17).

3.3. In vitro BL-PDT on 4T1 and MDA-MB-231 cells

We evaluated the intrinsic cytotoxicity of CTZ, Fuso-lip, and Luc-Ce6/Fuso-lip reagents with 4T1 (murine) and MDA-MB-231 (human) TNBC cell lines as well as L929 (mouse fibroblast) cells *in vitro* using a Cell Counting Kit-8 (CCK-8) assay (Fig. S18). No significant cytotoxicity was observed from all three cell types for 48 h, even with high concentrations of Luc-Ce6 (10 μM) and CTZ (100 μM).

Using the DCFDA intracellular assay, we detected considerable ROS generation in 4T1 cells after BL-PDT (10 μM Luc-Ce6, 100 μM CTZ) (Fig. 3a). The ROS level was comparable to that generated by conventional PDT (1 J cm^{-2}) using 4-times higher Ce6 amount (Fig. 3a). The DCFDA signal increased with an increasing amount of Luc-Ce6 for a fixed amount of CTZ (Fig. 3b, S19, and S20). BL-PDT resulted in near-complete cell killing confirmed by live/dead fluorescence dyes and morphological changes (Fig. 3c and S21-23). Cell killing by laser-PDT

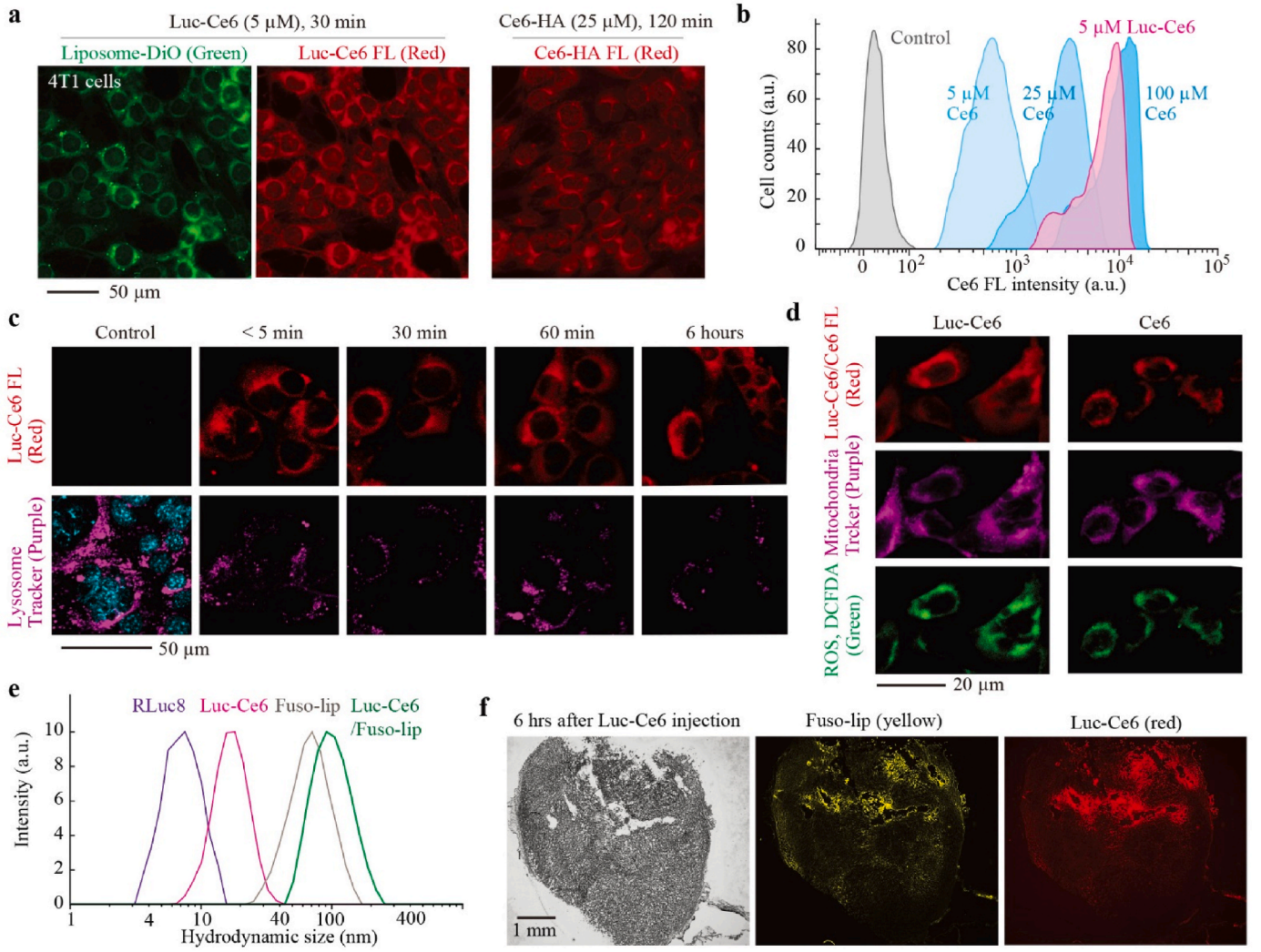

Fig. 2. Intracellular delivery of Luc-Ce6 conjugates. (a) Fluorescence images of 4T1 cells after incubation with 5 μM Luc-Ce6 (red)/Fuso-lip (green) for 30 min, or Ce6-HA molecules (25 μM) for 2 h. (b) Flow cytometry data of cells incubated with 5 μM Luc-Ce6/Fuso-lip and Ce6-HA with different concentrations. (c) Confocal fluorescence images of 4T1 cells after incubation with Luc-Ce6 (red)/Fuso-lip over time. Purple: lysosomes, blue: nucleus. (d) Confocal fluorescence images of Luc-Ce6/Fuso-lip-treated and Ce6-treated 4T1 cells. Purple: mitochondria, green: intracellular ROS. (e) The hydrodynamic sizes of the Luc protein, Luc-Ce6 conjugate, Fuso-lip, and Luc-Ce6/Fuso-lip. The final Fuso-lip with Luc-Ce6 is about 100 nm. (f) Fluorescence microscopy images of the whole tumor cryosection from the Luc-Ce6/Fuso-lip-treated mice. Fuso-lip: yellow, Luc-Ce6: red, BF: bright field. (For interpretation of the references to colour in this figure legend, the reader is referred to the Web version of this article.)

occurs only in regions illuminated with sufficient laser energy (Fig. 3c and S21). When we placed a layer of chicken breast tissues on top of cell samples in the optical path, simulating deep tissue therapy, no phototoxicity was observed, even with a modest tissue thickness of 300 μm (Fig. S24). Using the CCK-8 assay, we compared the dose-dependent cytotoxicity (Fig. 3d and e). The half-maximal inhibitory concentration (IC_{50}) values of Luc-Ce6 in BL-PDT were 5.56 μM for 4T1 cells and 1.51 μM for MDA-MB-231 cells. By comparison, IC_{50} values of Ce6 in laser-PDT were 20.8 μM for 4T1 and 5.39 μM for MDA-MB-231 cells, respectively. Moreover, we used an Annexin V-FITC/PI apoptosis detection kit and flow cytometry to confirm the apoptotic death of 4T1 cells 24 h after BL-PDT and laser-PDT (Fig. S26). In general, BL-PDT showed a considerable therapeutic effect *in vitro*.

3.4. *In vivo BL-PDT for TNBC tumors at the advanced stage*

For preclinical testing, we first established an orthotopic model of metastatic TNBC using ~10^6 4T1 cells in the mammary fat pad of a BALB/c mouse. The implanted tumor grew rapidly, reaching 4–5 mm in size in 1 week and 9–12 mm in 3 weeks (Fig. S27). Tumor invasion into surrounding tissues was observed on Day 14 (Fig. S27c). Consistently, no apparent metastasis was found in the sentinel lymph nodes (SLN) and lungs on Day 7. However, on Day 14, small metastases were detected in the SLNs and lungs (Fig. S28 and Fig. S29). On Day 21, multiple metastatic foci were evident throughout the lungs. For this result, we estimated that early metastasis occurs between 1 and 2 weeks.

We test the effect of BL PDT on relatively large-size tumors (7–8 mm). On Day 14, we injected Luc-Ce6/Fuso-lip into primary tumors, waited for 6 h for the Luc-Ce6 to diffuse into the tumor cells, and intravenously injected the first dose of CTZ (100 μM, 50 μl). Then, 5 additional injections of CTZ with the same dose were given in the subsequent 20 h (Fig. 4a). The tumors were harvested 3 days after the treatment. Their frozen tissue sections were examined using a terminal deoxynucleotidyl transferase dUTP nick-end labeling (TUNEL) assay to detect cell apoptosis. The BL-PDT treated groups showed strong TUNEL signals over larger areas and central locations (Fig. 4b). PBS-treated and Luc-Ce6 sham-treated tumors had no obvious TUNEL signals (Fig. 4c and S30). Laser-PDT treated groups, which had received the same intratumoral injection of Luc-Ce6/Fuso-lip and treated with a 405-nm laser (90 J cm^{-2}), showed TUNEL signals only in superficial regions along the

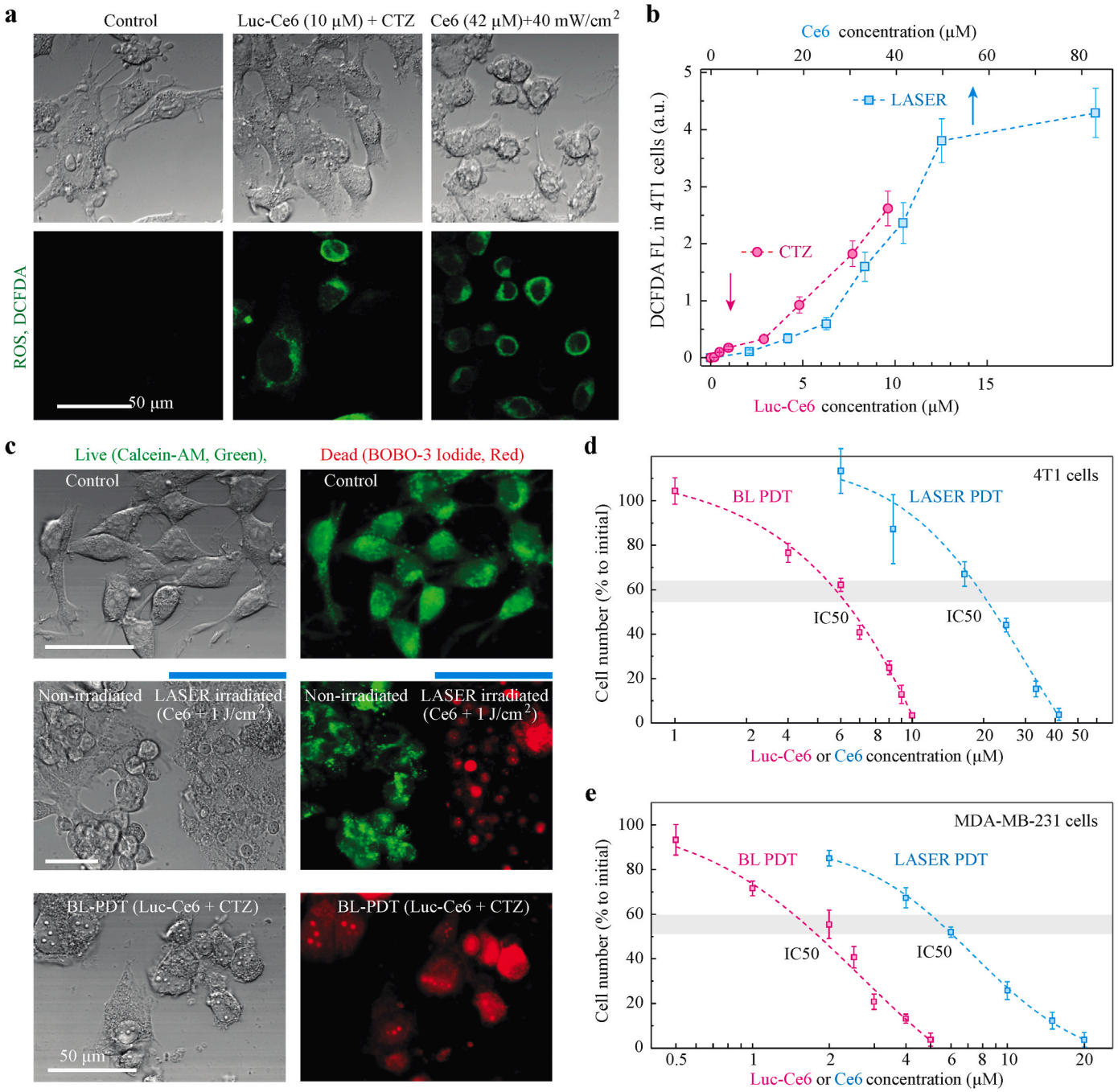

Fig. 3. ***In vitro*** **assessment of Luc-Ce6/Fuso-lip-based BL-PDT.** (a) Confocal microscopy images of intracellular ROS-sensing CDFDA (green) in 4T1 cells after BL-PDT (Luc-Ce6 10 μM and CTZ 100 μM) and laser-PDT (Ce6 and 405 nm laser, 1 J cm^{-2}). (b) Measured DCFDA intensity for BL-PDT and laser-PDT (1 J cm^{-2}) for various concentrations of Luc-Ce6 and Ce6. (c) Fluorescence images of 4T1 cells stained with Calcein AM (live cells, green) and BOBO-3 Iodide (dead cells, red). Scale bars, 50 μm. (d–e) Relative viability of 4T1 (d) and MDA-MB-231 cells (e) after BL-PDT and laser-PDT for different concentrations of Luc-Ce6 and Ce6. The horizontal grey band indicates the half-maximal inhibitory concentration (IC_{50}) levels. (For interpretation of the references to colour in this figure legend, the reader is referred to the Web version of this article.)

tumor boundary within <0.5 mm depth from the surface (Fig. 4e). This result showed the advantage of BL-PDT over laser-PDT in terms of therapeutic depth.

Neoadjuvant chemotherapy and radiation therapy are often performed before surgery to create conditions for better surgical resection for TNBC in the clinic [31,32]. We tested the neoadjuvant potential of BL-PDT for invasive tumors at the advanced stage (Fig. 4a). We injected Luc-Ce6/Fuso-lip at the root of the tumor around its boundary on Day 14 (Fig. 4e) and activated them in the tumor boundary by intravascularly administered CTZ (Fig. S31). 5 days after the BL-PDT, the tumors were collected for histological analysis. Most tumor cells in the border appeared round, atrophic, and apoptotic (Fig. 4f and S32). This morphological change visualized the margin more vividly than untreated tumors in control animals (Fig. 4d), in which the tumor invasion continued progressing. A laser-PDT-treated group also showed blurred tumor boundaries due to limited penetration depth of light (Fig. S33). Our result shows that neoadjuvant BL-PDT can act on deep tissue, shrink the tumor size, and delineate the tumor margin.

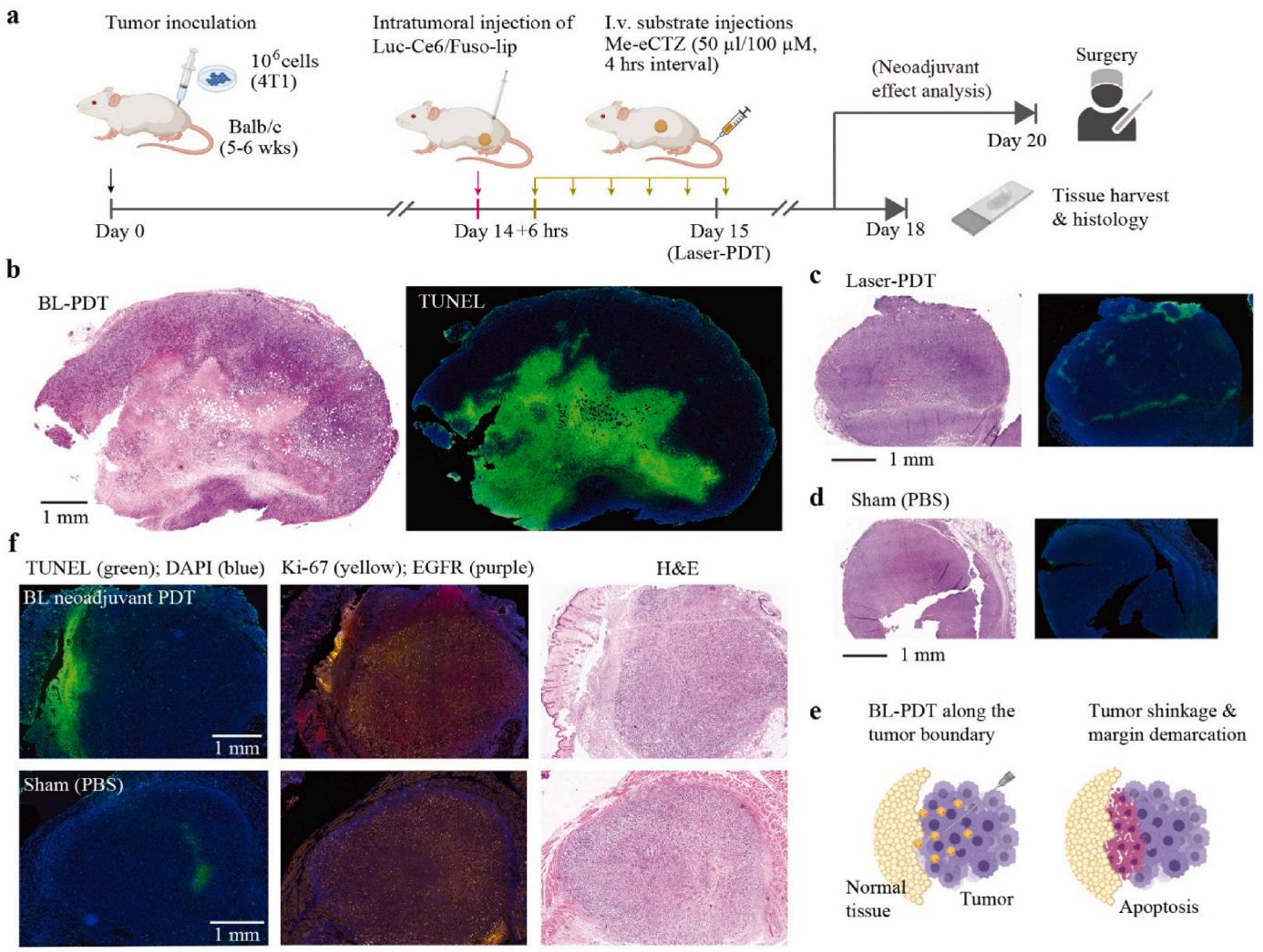

Fig. 4. *In vivo* assessment of BL-PDT in a 4T1 TNBC orthotopic model. (a) Schematic of the treatment schedule for 4T1 tumors at the advanced stage. (b–d) H&E and immunofluorescence (IF) images of tumor sections after BL-PDT treatment (b), laser-PDT (c, 405 nm, 90 J cm^{-2}), and PBS treatment (d). Green: TUNEL, blue: DAPI for nuclei. (e) Principle of neoadjuvant BL-PDT. (f) TUNEL, H&E, and IF-stained tumor sections, including surrounding normal tissues, 5 days after BL-PDT and sham (PBS) treatment. (For interpretation of the references to colour in this figure legend, the reader is referred to the Web version of this article.)

3.5. *In vivo* BL-PDT results in tumor regression and prevents metastasis

Having confirmed the cell-killing effect *in vivo*, we tested BL-PDT on tumors in their early stage of development. Fig. 5a depicts the treatment schedule. BL-PDT was applied on tumors 7 days after 4T1 cell inoculation, a time point when no metastasis is expected to have occurred. For BL-PDT-treated mice (n = 5), we measured the shrinkage of tumor volume within 2 days after treatment. Complete tumor regression was achieved by Day 18 without relapse (Fig. 5c). The body weights of the treated mice were normal (Fig. 5d). In stark contrast, laser-PDT-treated mice showed nearly unaffected exponential growth curves (Fig. 5b and c). Various organs were harvested on Day 25. Histology of tissue sections from the heart, liver, kidney, and spleen showed no sign of tissue damage (Fig. S34) nor metastasis in SLNs and lungs (Fig. 5f-g and S35). On Day 25, all the control, sham, and laser-PDT-treated mice showed substantial metastasis to the SLN and lung (Fig. 5e–g). Our result showed that BL-PDT could eradicate early-stage tumors and prevent metastasis in mice.

4. Discussion

The optimized Luc-Ce6 conjugates with high efficiency of utilizing self-luminescent biophotons and membrane-fusion liposomal delivery enabled us to demonstrate highly effective BL-PDT for *in vivo* treatments of TNBC. The molecularly activatable Luc-Ce6 conjugates enable depth-independent PDT, a significant advantage over conventional light-activatable photosensitizers. In addition, the all-natural-material reagents have no toxicity concerns. Therefore, they are more suitable for broad *in vivo* applications or clinical transformation than chemical luminal-based CL-PDT, typical inorganic nanoparticle-based BL-PDT, and Cerenkov radiation-induced PDT. Additionally, the inherent highly therapeutic performance of Luc-Ce6 conjugate, owing to the adequate use of bio-photons, enables a more substantial therapeutic effect *in vivo*, compared with recently synthetic protein-based BL-PDT. Furthermore, the triggerable action of CTZ substrate allows BL-PDT to be performed at a desired time when the reagents have been delivered to target regions for the best therapeutic outcome. It also helps to achieve low background cytotoxicity, an advantage over non-activable drugs like conventional chemotherapy agents.

The ROS-mediated mechanism makes PDT a unique modality different from chemotherapies, radiation therapies, and immunotherapies [33,34]. Our results demonstrated the potential of BL-PDT as a standalone, complementary, or synergistic treatment option for cancer treatment used like a typical pharmaceutic agent. In this study, we have investigated intratumoral delivery by local injection of Luc-Ce6/Fuso-lip. Although this method could be viable for treating

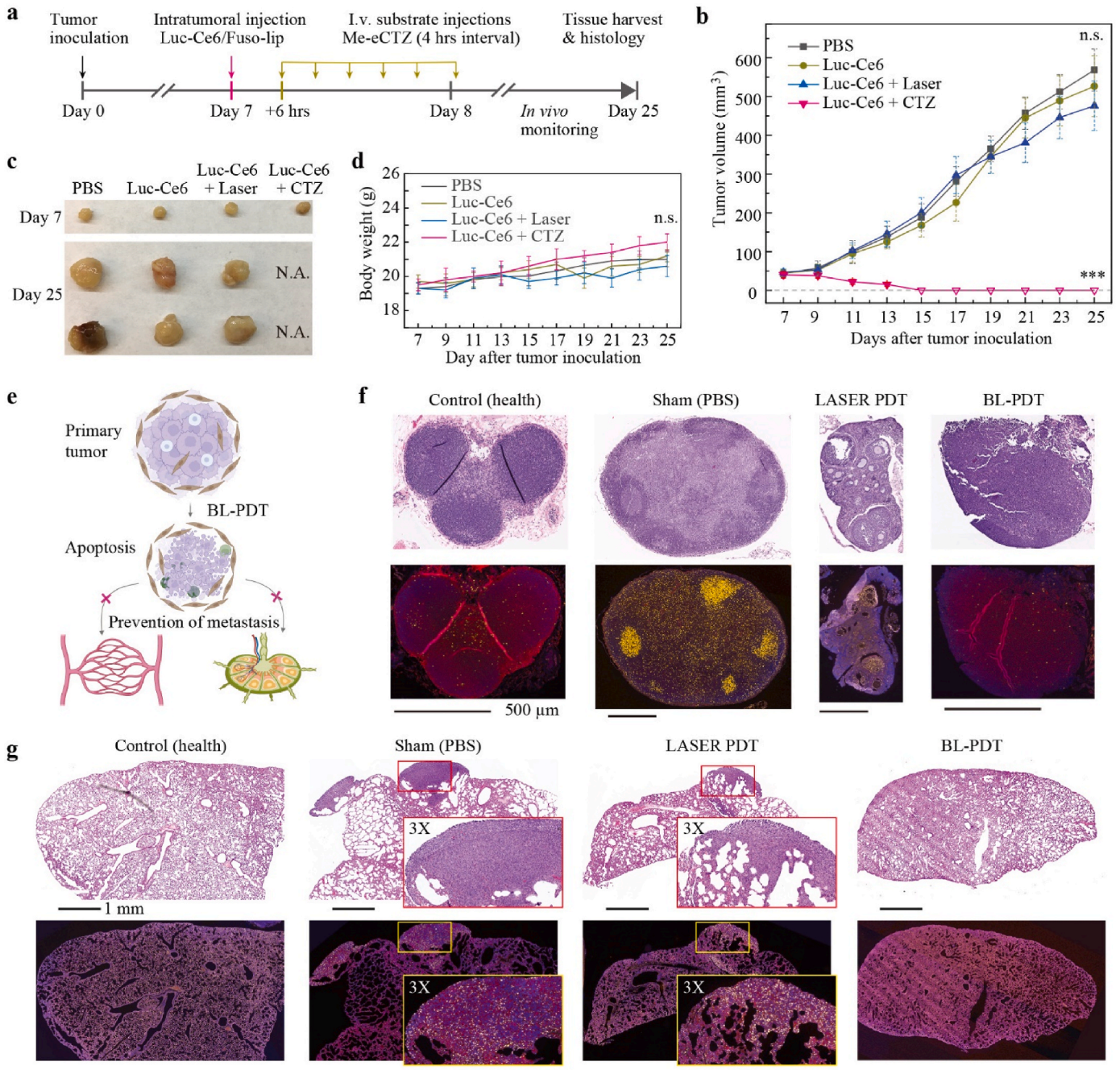

Fig. 5. The effects of BL-PDT on early-stage 4T1 tumor. (a) Treatment schedule. (b) Growth curves of tumors in different groups: PBS injection only, Luc-Ce6 injection only, Luc-Ce6 and laser activation (laser-PDT, 405 nm, 90 J cm^{-2}), and Luc-Ce6 and substrate CTZ activation (BL-PDT). Error bars are the standard deviation of 5 animals per group. ***, $P < 0.001$; n. s.: not significant. (c) Photos of tumors harvested from different groups at different times. (d) Body weight. (e) Illustration of BL-PDT inducing apoptosis of the primary tumor and preventing metastasis to the lung and sentinel lymph node. (f–g) H&E histology and immunofluorescence (IF)-stained sentinel lymph nodes (f) and lungs (g) harvested from tumor-bearing mice at 18 days: healthy mice, PBS injection only (sham), laser-PDT, and BL-PDT. Blue: DAPI, yellow: Ki-67 (nucleus), red: EGFR (cell membrane). While metastasis is apparent in the lymph nodes and lungs in the PBS and laser-PDT groups, no evident metastasis was found in the control and BL-PDT groups. (For interpretation of the references to colour in this figure legend, the reader is referred to the Web version of this article.)

small tumors or neo-adjuvant treatment of larger tumors, as demonstrated, it will be worthwhile to develop an excellent systemic delivery method of BRET conjugates for broader applications such as treating metastases because the therapeutic effect of BL-PDT dramatically relies on the amount of Luc-Ce6 aggregation [35,36]. Exploring different all-natural luciferases, luciferins, and photosensitizers for different target tissues and organelles will also be interesting. In addition, BL-PDT can apply to treat non-cancers, such as deep skin lesions. Finally, the BRET strategy may be extended to other phototherapies, such as antibacterial blue light therapies that use endogenous photosensitizers [37,38]. Our promising results encourage further developments toward clinical BRET-based phototherapies.

Credit author statement

Hao Yan: designed the experiments together, fabricated Luc-Ce6

conjugates, developed fusion liposomal delivery, conducted *in vitro* experiments, established the mouse model, performed *in vivo* experiments, prepared figures, and wrote the manuscript together. Sarah Forward: developed fusion liposomal delivery and established the mouse model. Kwon-Hyeon Kim: fabricated Luc-Ce6 conjugates. Yue Wu: assisted in chemistry. Jie Hui: assisted in chemistry. Anokhi Kashiparekh: performed biocompatibility assays. Seok-Hyun Yun: PI and funding supporter, designed the experiments, prepared figures, and wrote the manuscript together.

Declaration of competing interest

The authors declare that they have no known competing financial interests or personal relationships that could have appeared to influence the work reported in this paper.

Data availability

Data will be made available on request.

Acknowledgments

This work was supported by the US National Institutes of Health (NIH) grant, 5R01CA192878, and the Human Frontier Science Program (HFSP, RGP0034/2016). We thank Drs. Tayyaba Hasan and Seonghoon Kim for contributions in the initial stage of the project, Dr. Burkhard Ludwig for discussion, and Dr. Jenny Zhao and the Wellman Photopathology Core for helping with tissue sectioning, staining, and imaging.

Appendix A. Supplementary data

Supplementary data to this article can be found online at https://doi.org/10.1016/j.biomaterials.2023.122079.

References

[1] J.P. Celli, B.Q. Spring, I. Rizvi, C.L. Evans, K.S. Samkoe, S. Verma, B.W. Pogue, T. Hasan, Imaging and photodynamic therapy: mechanisms, monitoring, and optimization, Chem. Rev. 110 (5) (2010) 2795–2838.
[2] S.H. Yun, S.J.J. Kwok, Light in diagnosis, therapy and surgery, Nat. Biomed. Eng. 1 (1) (2017) 1–16.
[3] M. Mitsunaga, M. Ogawa, N. Kosaka, L.T. Rosenblum, P.L. Choyke, H. Kobayashi, Cancer cell-selective in vivo near infrared photoimmunotherapy targeting specific membrane molecules, Nat. Med. 17 (12) (2011) 1685–1692.
[4] N.M. Idris, M.K. Gnanasammandhan, J. Zhang, P.C. Ho, R. Mahendran, Y. Zhang, In vivo photodynamic therapy using upconversion nanoparticles as remote-controlled nanotransducers, Nat. Med. 18 (10) (2012) 1580–1586.
[5] J.J. He, Y. Wang, M.A. Missinato, E. Onuoha, L.A. Perkins, S.C. Watkins, C.M. St Croix, M. Tsang, M.P. Bruchez, A genetically targetable near-infrared photosensitizer, Nat. Methods 13 (3) (2016) 263–271.
[6] H.Y. Huang, B.L. Yu, P.Y. Zhang, J.J. Huang, Y. Chen, G. Gasser, L.N. Ji, H. Chao, Highly charged ruthenium(II) polypyridyl complexes as lysosome-localized photosensitizers for two-photon photodynamic therapy, Angew. Chem. Int. Ed. 54 (47) (2015) 14049–14052.
[7] R. Gao, X. Mei, D.P. Yan, R.Z. Liang, M. Wei, Nano-photosensitizer based on layered double hydroxide and isophthalic acid for singlet oxygenation and photodynamic therapy, Nat. Commun. 9 (1) (2018) 1–10.
[8] N. Kotagiri, G.P. Sudlow, W.J. Akers, S. Achilefu, Breaking the depth dependency of phototherapy with Cerenkov radiation and low-radiance-responsive nanophotosensitizers, Nat. Nanotechnol. 10 (4) (2015) 370–379.
[9] X.Q. Xu, H.J. An, D.L. Zhang, H. Tao, Y. Dou, X.H. Li, J. Huang, J.X. Zhang, A self-illuminating nanoparticle for inflammation imaging and cancer therapy, Sci. Adv. 5 (1) (2019), eaat2953.
[10] J. Jeon, D.G. You, W. Um, J. Lee, C.H. Kim, S. Shin, S. Kwon, J.H. Park, Chemiluminescence resonance energy transfer-based nanoparticles for quantum yield-enhanced cancer phototheranostics, Sci. Adv. 6 (21) (2020) eaaz8400.
[11] C. Lu, C. Zhang, P. Wang, Y. Zhao, Y. Yang, Y. Wang, H. Yuan, S. Qu, X. Zhang, G. Song, K. Pu, Light-free generation of singlet oxygen through manganese-thiophene nanosystems for pH-responsive chemiluminescence imaging and tumor therapy, Chem 6 (9) (2020) 2314–2334.
[12] Z. Yu, P. Zhou, W. Pan, N. Li, B. Tang, A biomimetic nanoreactor for synergistic chemiexcited photodynamic therapy and starvation therapy against tumor metastasis, Nat. Commun. 9 (1) (2018) 1–9.
[13] C.Y. Hsu, C.W. Chen, H.P. Yu, Y.F. Lin, P.S. Lai, Bioluminescence resonance energy transfer using luciferase-immobilized quantum dots for self-illuminated photodynamic therapy, Biomaterials 34 (4) (2013) 1204–1212.
[14] Y.R. Kim, S. Kim, J.W. Choi, S.Y. Choi, S.H. Lee, H. Kim, S.K. Hahn, G.Y. Koh, S. H. Yun, Bioluminescence-activated deep-tissue photodynamic therapy of cancer, Theranostics 5 (8) (2015) 805–817.
[15] Y.K. Yang, W.Y. Hou, S.Y. Liu, K. Sun, M.Y. Li, C.F. Wu, Biodegradable polymer nanoparticles for photodynamic therapy by bioluminescence resonance energy transfer, Biomacromolecules 19 (1) (2018) 201–208.
[16] E.H. Kim, S. Park, Y.K. Kim, M. Moon, J. Park, K.J. Lee, S. Lee, Y.P. Kim, Self-luminescent photodynamic therapy using breast cancer targeted proteins, Sci. Adv. 6 (37) (2020), eaba3009.
[17] E.I. Shramova, S.P. Chumakov, V.O. Shipunova, A.V. Ryabova, G.B. Telegin, A. V. Kabashin, S.M. Deyev, G.M. Proshkina, Genetically encoded BRET-activated photodynamic therapy for the treatment of deep-seated tumors, Light Sci. Appl. 11 (1) (2022) 1–13.
[18] A. Roda, M. Guardigli, Analytical chemiluminescence and bioluminescence: latest achievements and new horizons, Anal. Bioanal. Chem. 402 (1) (2012) 69–76.
[19] S.F. Leechen, C.T. Yu, D.R. Wu, K.Y. Jan, DIFFERENTIAL-EFFECTS of luminol, nickel, and arsenite on the rejoining of ultraviolet-light and alkylation-induced DNA breaks, Mol. Mutagen. 23 (2) (1994) 116–120.
[20] A.M. Loening, T.D. Fenn, A.M. Wu, S.S. Gambhir, Consensus guided mutagenesis of Renilla luciferase yields enhanced stability and light output, Protein Eng. Des. Sel. 19 (9) (2006) 391–400.
[21] A.M. Loening, T.D. Fenn, S.S. Gambhir, Crystal structures of the luciferase and green fluorescent protein from Renilla reniformis, J. Mol. Biol. 374 (4) (2007) 1017–1028.
[22] J.D. Spikes, J.C. Bommer, Photosensitizing properties of mono-l-aspartyl chlorin E (6) (NPE6) - a candidate sensitizer for the photodynamic therapy of tumors, J. Photochem. Photobiol. B Biol. 17 (2) (1993) 135–143.
[23] K. Kasuya, M. Shimazu, M. Suzuki, Y. Kuroiwa, J. Usuda, T. Itoi, A. Tsuchida, T. Aoki, Novel photodynamic therapy against biliary tract carcinoma using mono-l-aspartyl chlorine e6: basic evaluation for its feasibility and efficacy, J Hepatobiliary Pancreat Sci. 17 (3) (2010) 313–321.
[24] X. Ragas, A. Jimenez-Banzo, D. Sanchez-Garcia, X. Batllori, S. Nonell, Singlet oxygen photosensitisation by the fluorescent probe singlet oxygen sensor green (R), Chem. Commun. 20 (2009) 2920–2922.
[25] B. Kim, H.B. Pang, J. Kang, J.H. Park, E. Ruoslahti, M.J. Sailor, Immunogene therapy with fusogenic nanoparticles modulates macrophage response to Staphylococcus aureus, Nat. Commun. 9 (1) (2018) 1–11.
[26] J.A. Zuris, D.B. Thompson, Y. Shu, J.P. Guilinger, J.L. Bessen, J.H. Hu, M. L. Maeder, J.K. Joung, Z.Y. Chen, D.R. Liu, Cationic lipid-mediated delivery of proteins enables efficient protein-based genome editing in vitro and in vivo, Nat. Biotechnol. 33 (1) (2015) 73–80.
[27] S. Behzadi, V. Serpooshan, W. Tao, M.A. Hamaly, M.Y. Alkawareek, E.C. Dreaden, D. Brown, A.M. Alkilany, O.C. Farokhzad, M. Mahmoudi, Cellular uptake of nanoparticles: journey inside the cell, Chem. Soc. Rev. 46 (14) (2017) 4218–4244.
[28] S.I. Choi, Y.S. Maeng, T.I. Kim, Y. Lee, Y.S. Kim, E.K. Kim, Lysosomal trafficking of TGFBIp via caveolae-mediated endocytosis, PLoS One 10 (4) (2015), e0119561.
[29] M.R. Hamblin, J.L. Miller, I. Rizvi, B. Ortel, E.V. Maytin, T. Hasan, Pegylation of a chlorin(e6) polymer conjugate increases tumor targeting of photosensitizer, Cancer Res. 61 (19) (2001) 7155–7162.
[30] D. Kessel, N.L. Oleinick, Cell death pathways associated with photodynamic therapy: an update, Photochem. Photobiol. 94 (2) (2018) 213–218.
[31] A. Cinkaya, M. Akin, A. Sengul, Evaluation of treatment outcomes of triple-negative breast cancer, J. Cancer Res. Therapeut. 12 (1) (2016) 150–154.
[32] M.C. Bourgeois-Daigneault, D.G. Roy, A.S. Aitken, N. El Sayes, N.T. Martin, O. Varette, T. Falls, L.E. St-Germain, A. Pelin, B.D. Lichty, D.F. Stojdl, G. Ungerechts, J.S. Diallo, J.C. Bell, Neoadjuvant oncolytic virotherapy before surgery sensitizes triple- negative breast cancer to immune checkpoint therapy, Sci. Transl. Med. 10 (422) (2018), eaao1641.
[33] C.H. Liu, Y. Cao, Y.R. Cheng, D.D. Wang, T.L. Xu, L. Su, X.J. Zhang, H.F. Dong, An open source and reduce expenditure ROS generation strategy for chemodynamic/photodynamic synergistic therapy, Nat. Commun. 11 (1) (2020) 1–9.
[34] G.C. Yu, S. Yu, M.L. Saha, J. Zhou, T.R. Cook, B.C. Yung, J. Chen, Z.W. Mao, F. W. Zhang, Z.J. Zhou, Y.J. Liu, L. Shao, S. Wang, C.Y. Gao, F.H. Huang, P.J. Stang, X.Y. Chen, A discrete organoplatinum(II) metallacage as a multimodality theranostic platform for cancer photochemotherapy, Nat. Commun. 9 (1) (2018) 1–18.
[35] Z.M. Zhao, A. Ukidve, J. Kim, S. Mitragotri, Targeting strategies for tissue-specific drug delivery, Cell 181 (1) (2020) 151–167.
[36] R. van der Meel, E. Sulheim, Y. Shi, F. Kiessling, W.J.M. Mulder, T. Lammers, Smart cancer nanomedicine, Nat. Nanotechnol. 14 (11) (2019) 1007–1017.
[37] Y.C. Wang, Y. Wang, Y.G. Wang, C.K. Murray, M.R. Hamblin, D.C. Hooper, T. H. Dai, Antimicrobial blue light inactivation of pathogenic microbes: state of the art, Drug Resist. Updates 33 (35) (2017) 1–22.
[38] J. Hui, P.T. Dong, L.J. Liang, T. Mandal, J.J. Li, E.R. Ulloa, Y.W. Zhan, S. Jusuf, C. Zong, M.N. Seleem, G.Y. Liu, Q. Cui, J.X. Cheng, Photo-disassembly of membrane microdomains revives conventional antibiotics against MRSA, Adv. Sci. 7 (6) (2020), 1903117.

Supplementary Information

All-natural-molecule, bioluminescent photodynamic therapy results in complete tumor regression and prevents metastasis

Hao Yan,[1] Sarah Forward,[1] Kwon-Hyeon Kim,[1] Yue Wu,[1] Jie Hui,[1] Anokhi Kashiparekh,[1] Seok-Hyun Yun[1,*]

[1]Harvard Medical School and Wellman Center for Photomedicine, Massachusetts General Hospital, 65 Landsdowne St., UP-5, Cambridge, MA 02139, USA

*Correspondence: syun@hms.harvard.edu

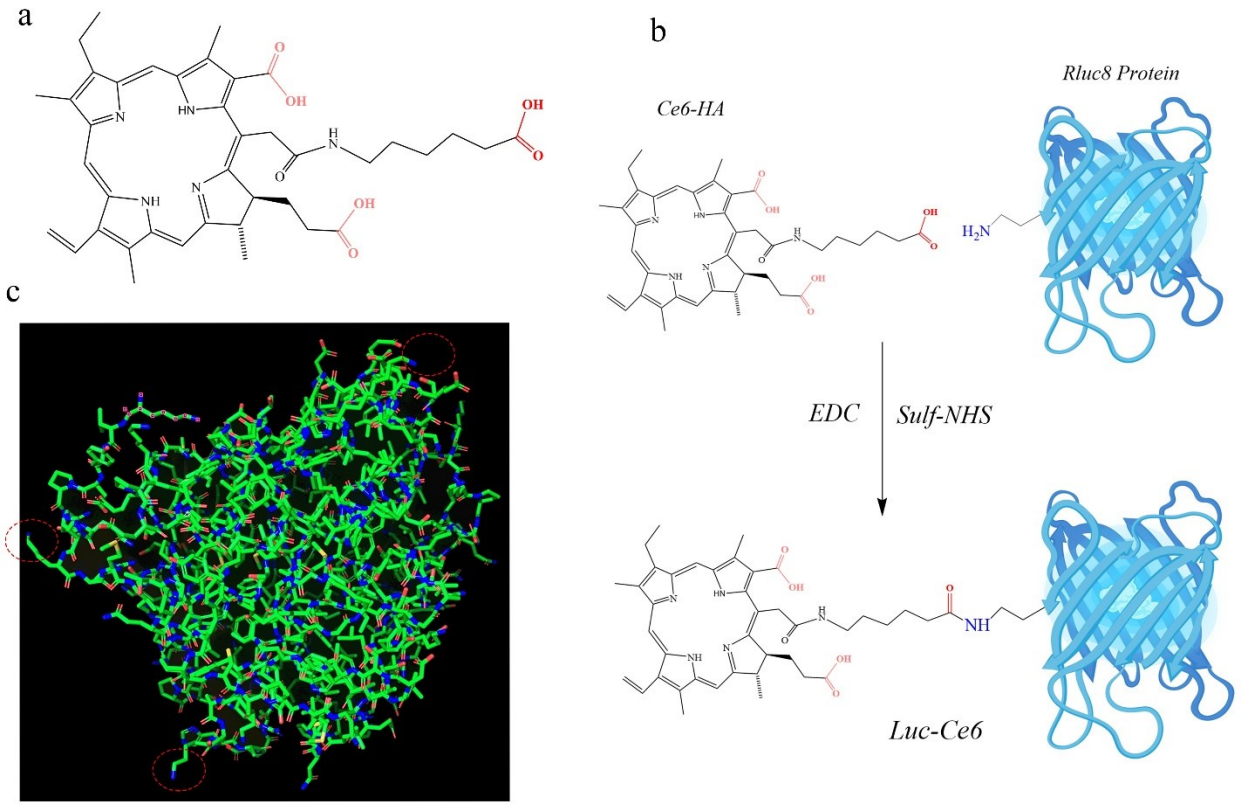

Figure S1. Structure of Ce6-HA molecule, RLuc8 (Luc) protein, and Luc-Ce6 conjugate. (a) Chemical structure of Ce6-HA. The carboxyl group at the end of the long side chain can react with the amino group on the RLuc8 protein surface. (b) Synthesis steps of the Luc-Ce6 conjugate. The carboxyl group is modified by EDC and Sulfo-NHS first and then conjugated with Luc in DPBS buffer at room temperature. (c) A 3D model of the RLuc8 protein [(1)]. A few amino groups (blue symbols and dashed circle) are exposed at the periphery. [(1)] Crystal Structures of the Luciferase and Green Fluorescent Protein from Renilla Reniformis. 2PSD: PCSB/PDB.

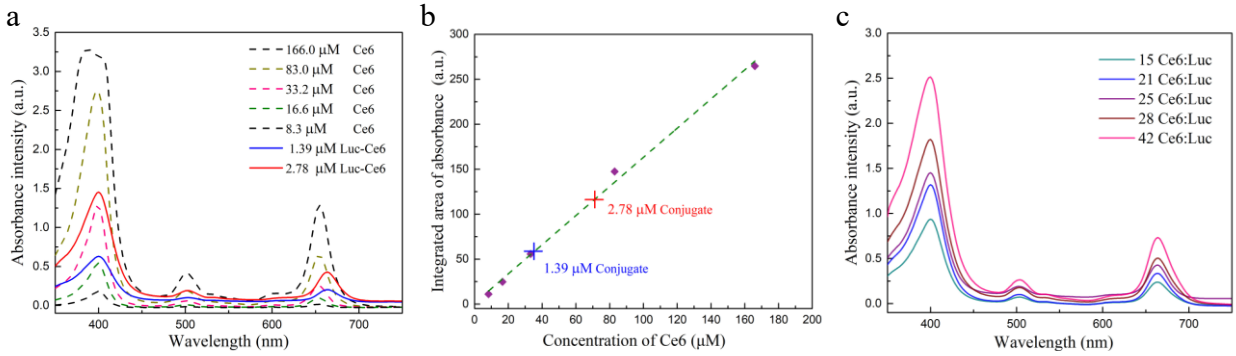

Figure S2. The absorption characteristics of Ce6-HA molecules and Luc-Ce6 conjugates. (a) Absorption spectra of Ce6-HA (dashed lines) and Luc-Ce6 (solid lines) at different concentrations in solution. (b) The area under the curve (absorption) for the Luc-Ce6 and Ce6-HA solutions with different Ce6 concentrations. The conjugation mole ratio of Ce6-HA to Luc is determined to be ~ 25 (25.04 from 1.39 μM and 25.34 from 2.78 μM samples). (c) Absorption spectra of Luc-Ce6 with different mole conjugation ratios of Ce6-HA molecules to Luc protein.

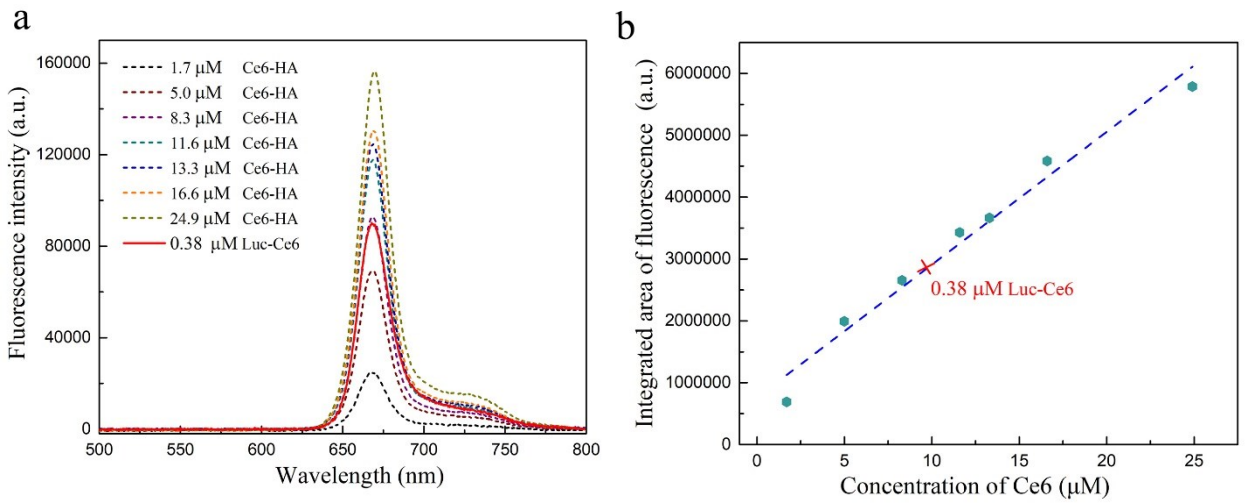

Figure S3. The fluorescence characteristics of Luc-Ce6. (a) Fluorescence spectra of Ce6-HA with different concentrations (dashed lines) and Luc-Ce6 conjugate (red line) in solution. (b) The area under the curve (fluorescence) for Luc-Ce6 and Ce6-HA solutions with different concentrations of Ce6 (or Ce6-HA). From the comparison, the conjugation mole ratio of Ce6-HA to Luc is determined to be ~ 25 (24.78).

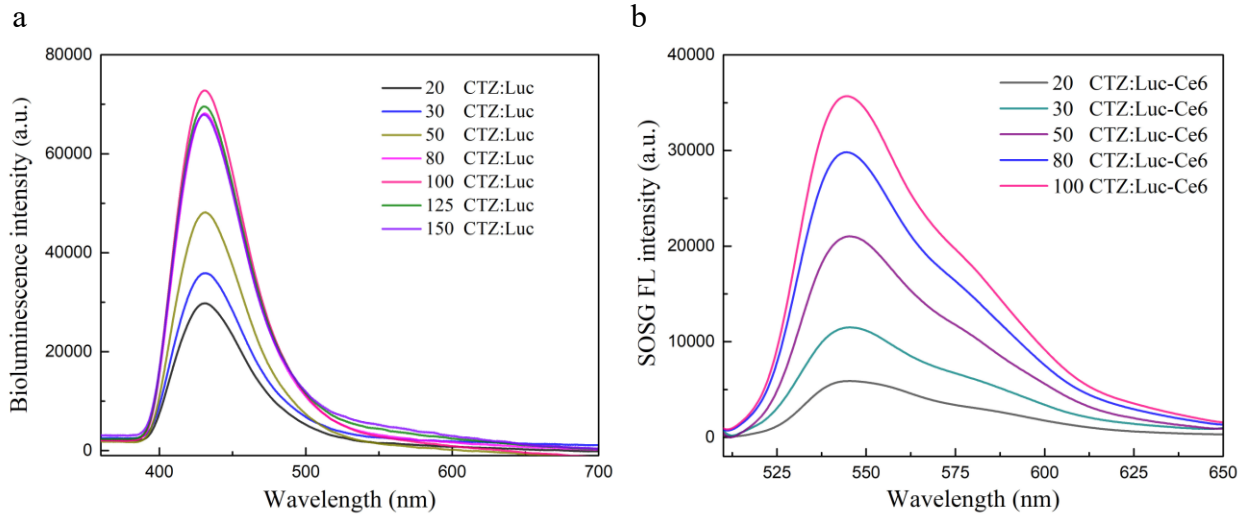

Figure S4. Bioluminescence spectrum and Singlet Oxygen Sensor Green (SOSG) fluorescence spectrum of Luc-Ce6 conjugate after adding different molar ratios of substrates. (a) The bioluminescence spectrum of Luc-Ce6 conjugate (0.3 μM) after different molar ratios of substrates was added to activate (from 20 to 150). (b) SOSG FL spectrum of Luc-Ce6 conjugate solution (2.78 μM) with different molar ratios of substrates.

Table S1. BRET ratio in emission, and the probability of activating Ce6 per BL photon via BRET.

	A (photons)	B (photons)	BRET ratio (emission)	Number of activated Ce6	Ce6 activation / BL photon
Method	Integration over 400-600 nm	Integration over 600-800 nm	B / A	B / Ce6 quantum yield, 0.15[(2)]	Activated Ce6 / A0
Luc8 only	2,690,000 (= **A0**)	0	0	0	0
Luc-Ce6 conjugate	454,000	323,000	0.71	2,153,000	**80.07%**
Simple mixture of Luc and Ce6	1,120,000	172,000	0.15	1,146,700	42.65%

[(2)] Kay A, Humphrybaker R, Gratzel M. Artificial Photosynthesis. 2. Investigations on the Mechanism of Photosensitization of Nanocrystalline TiO_2 Solar Cells by Chlorophyll Derivatives. *Journal of Physical Chemistry* **98**, 952-959 (1994).

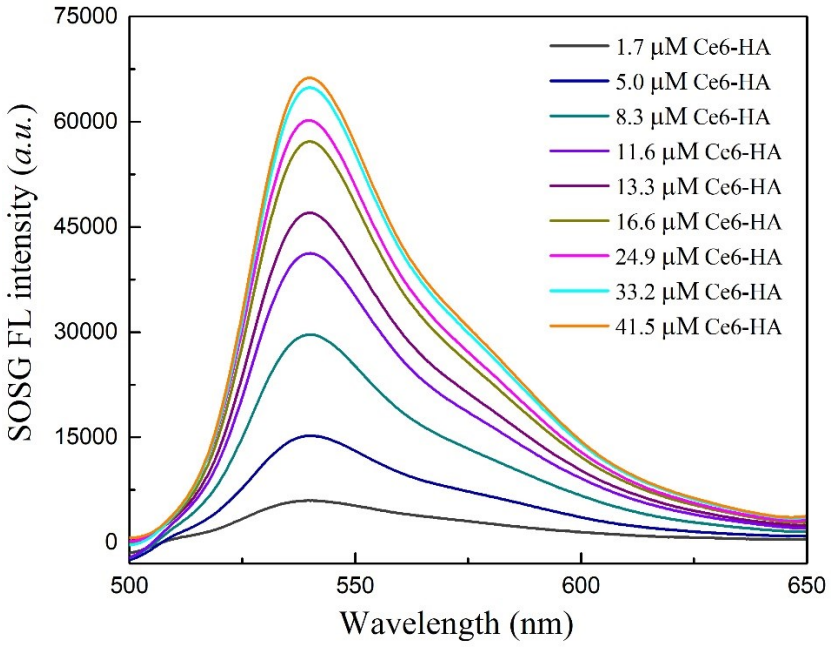

Figure S5. Fluorescence signals from a mixture of Singlet Oxygen Sensor Green (SOSG) dye and Ce6-HA with different concentrations after being excited by 405 nm laser with a dose of 1 J cm^{-2}.

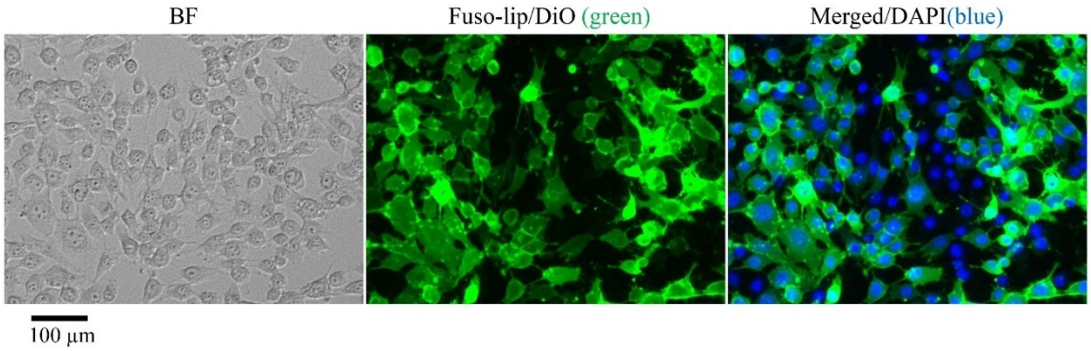

Figure S6. Fluorescence confocal images of 4T1 cells after incubation with fusogenic nano-liposomes (Fuso-lip, green) for 30 min. Nucleus were stained with DAPI (blue). Fusogenic nano-liposomes marked by DiO dyes (ex/em = 484/501 nm) fuses with the cell membrane immediately.

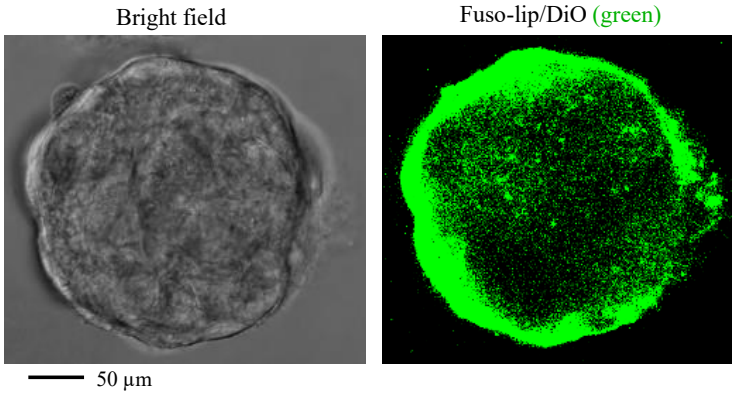

Figure S7. A fluorescence confocal image of Fuso-lip (green) that has penetrated a three-dimensional 4T1 tumor spheroid after incubation for 4 hrs. The relatively dim fluorescence intensity in the middle of spheroid is largely due to the limited penetration depth of confocal microscopy.

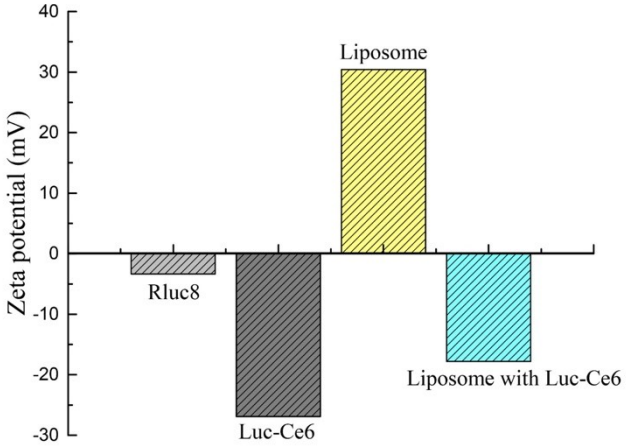

Figure S8. The Zeta potential of free Luc proteins (-3.37 mV), Luc-Ce6 conjugates (-26.9 mV), fusogenic nano-liposomes (+30.4 mV), and Luc-Ce6/Fuso-lip (-17.8 mV).

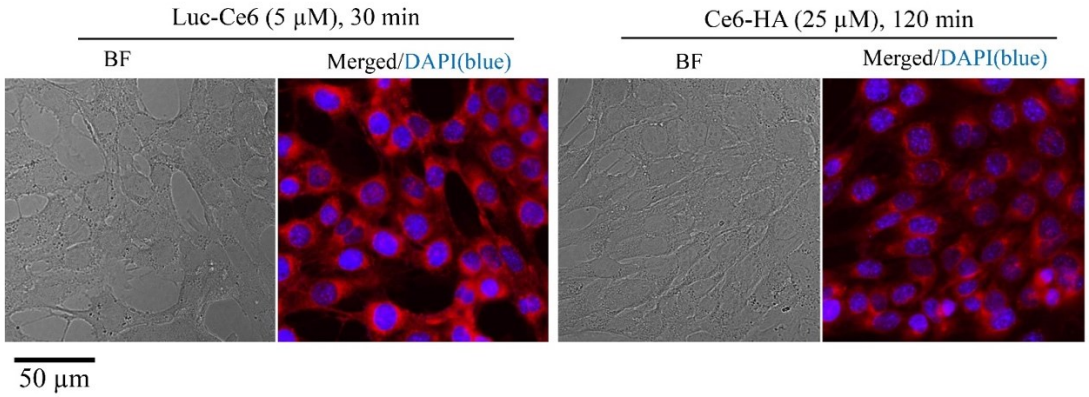

Figure S9. Bright-field (BF) and fluorescence confocal images of 4T1 cells after incubation with 5 μM Luc-Ce6 (red)/Fuso-lip (green) for 30 min (left) and Ce6-HA molecules (25 μM) for 2 hrs. (right). The cell nuclei are stained with DAPI (blue).

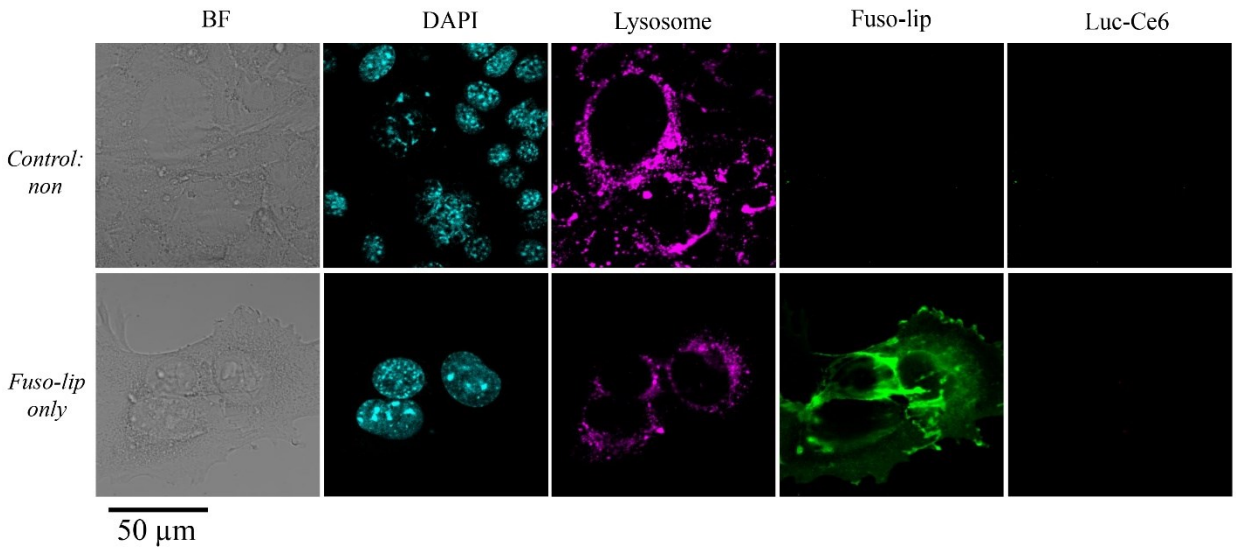

Figure S10. Confocal fluorescence images of 4T1 cells after incubation with Fuso-lip for 30 min. The lysosomes were stained with Lysosome Tracker (purple), and the cell nuclei were stained with DAPI (blue). The distribution of the Fuso-lip has low correlation with the locations of lysosomes.

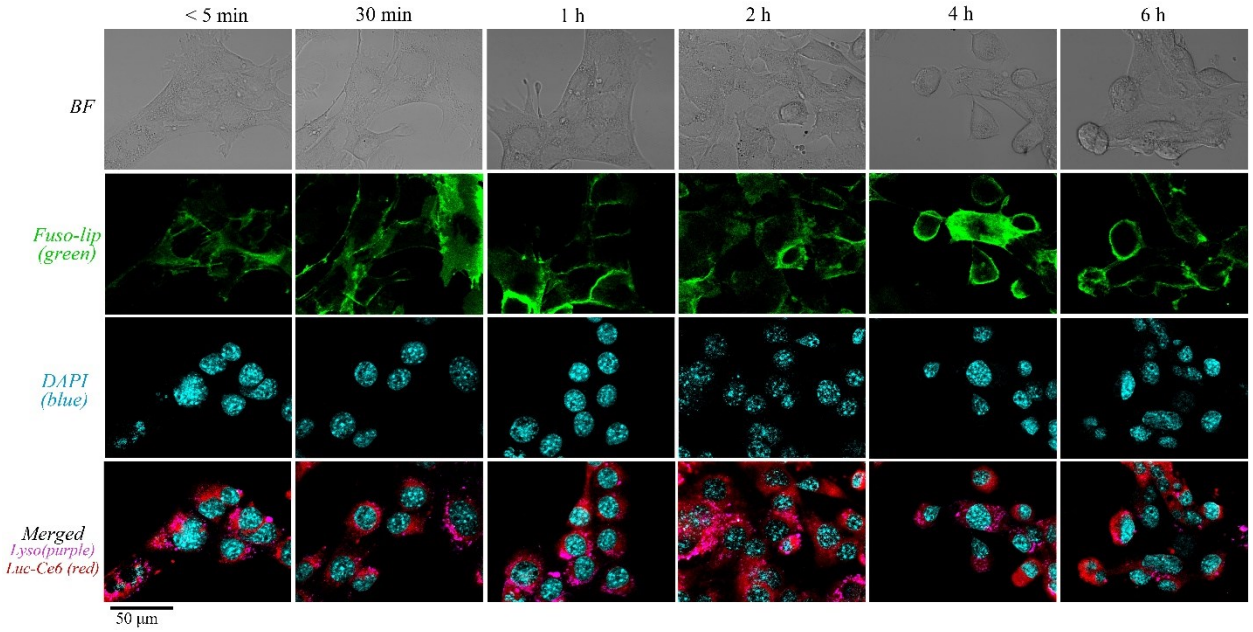

Figure S11. Confocal fluorescence images of 4T1 cells at different duration of incubation with Luc-Ce6 (red)/Fuso-lip. The lysosomes were stained by Lysosome Tracker (purple), and the cell nuclei were stained with DAPI (blue). Cells were incubated with Luc-Ce6/ Fuso-lip for 30 min, then washed, stained with the fluorescent probes, and fixed.

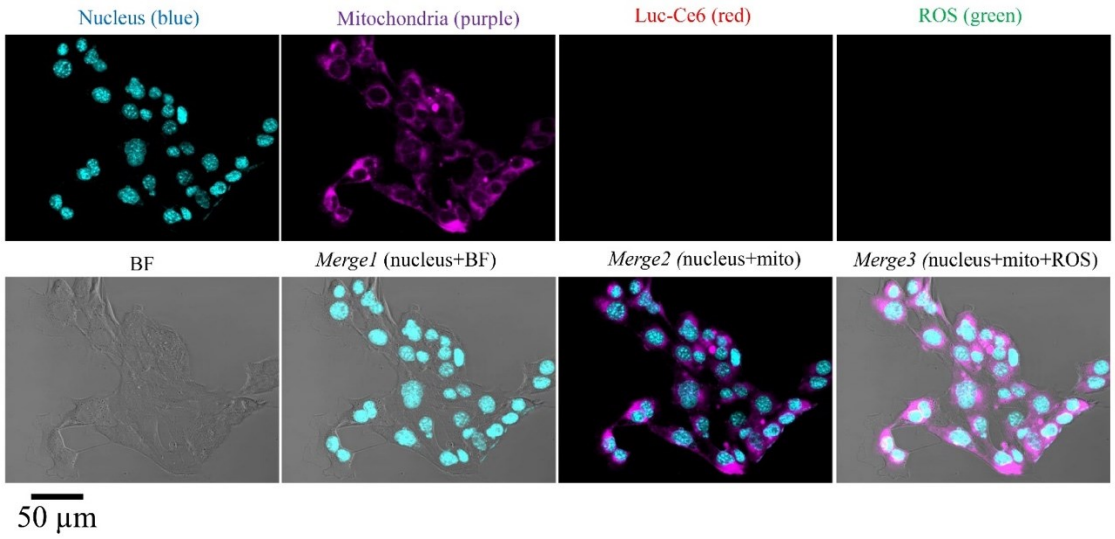

Figure S12. Confocal fluorescence images of 4T1 cells, stained for mitochondria (purple, mitochondria tracker) and intracellular ROS (green, DCFDA).

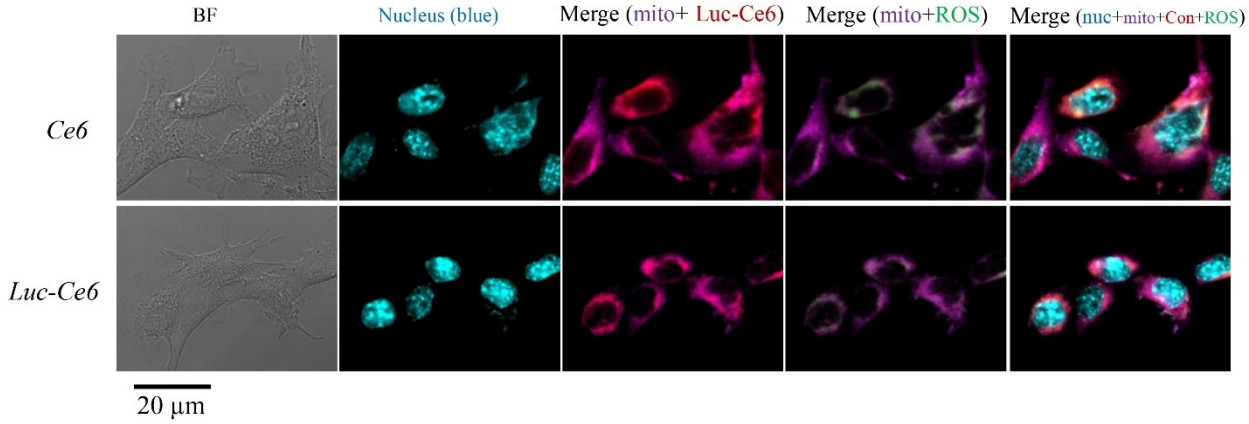

Figure S13. Confocal fluorescence images of 4T1 cells after laser-PDT (top rows) and BL-PDT (bottom rows), stained for mitochondria (purple) and intracellular ROS (green, DCFDA).

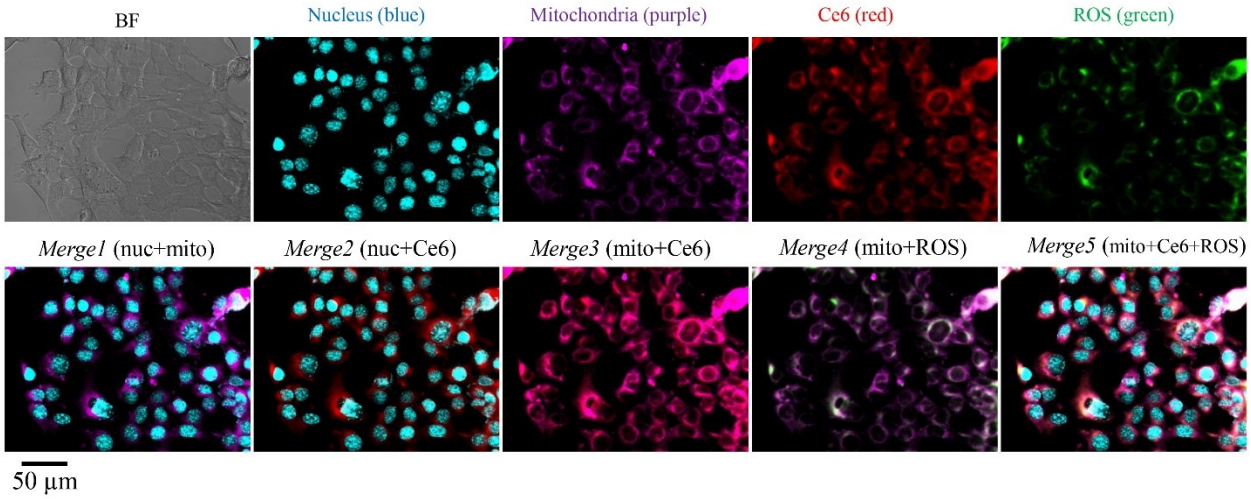

Figure S14. Confocal fluorescence images of 4T1 cells after laser-PDT (41.5 μM Ce6 for 1 h incubation and 405 nm illumination with a dose of 1 J/cm^2). Mitochondria were stained with a Mitochondria tracker kit, intracellular ROS with DCFDA, nucleus with DAPI.

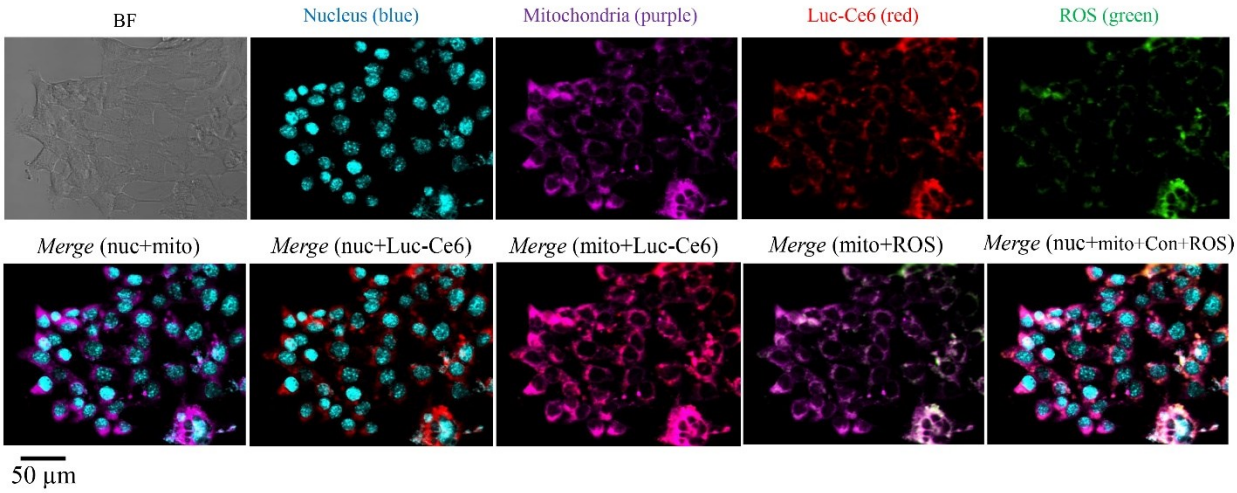

Figure S15. Confocal fluorescence images of 4T1 cells after BL-PDT (5 μM Luc-Ce6/Fuso-lip with 30 min incubation and then 100 μM CTZ with 4 hrs. incubation). The distribution of mitochondria, ROS, and Ce6 (in Luc-Ce6) are apparently similar to the result in laser-PDT in Fig. 14.

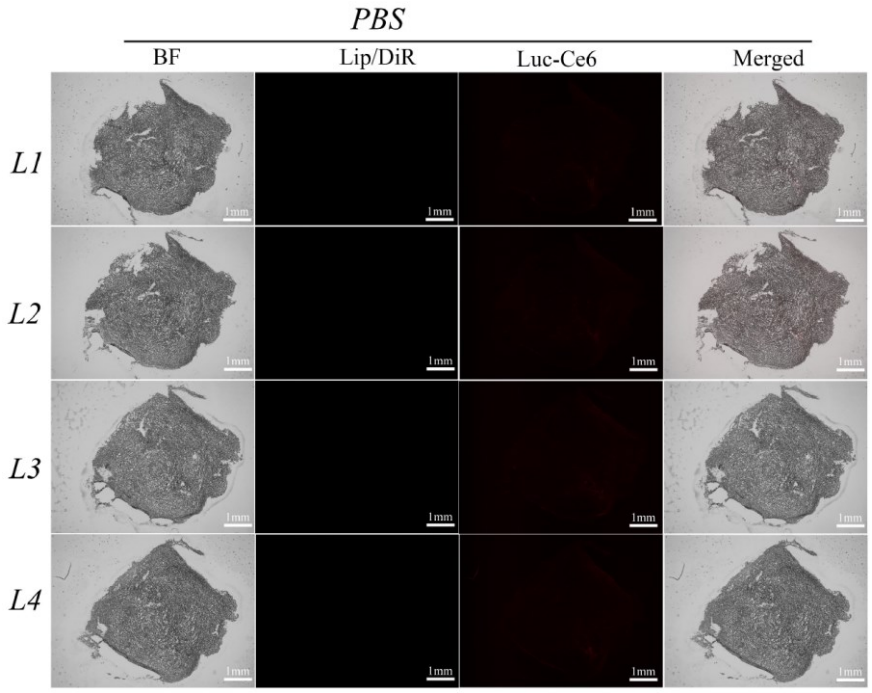

(Control, see next page)

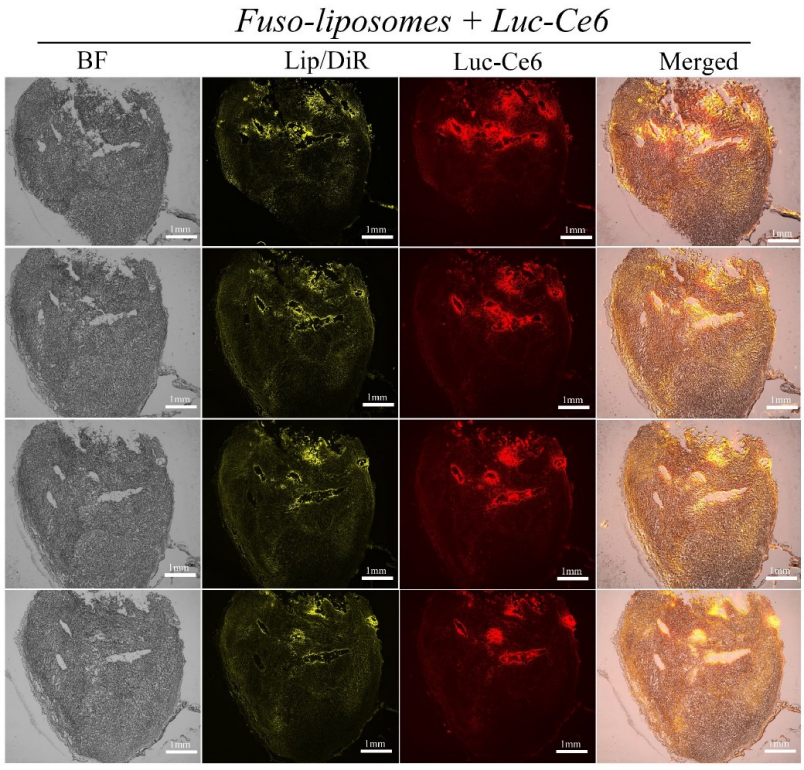

Figure S16. Multi-layer biodistribution of Luc-Ce6 and Fuso-lip injected into an advanced 4T1 tumor *in vivo* with a size of 4-5 mm. Four layers (L1 to L4) of the frozen-sectioned tumor tissue, with spacing of 50 μm between layers, are shown. Fuso-lip and Luc-Ce6 conjugates are extensively, not uniformly, distributed in the tumor.

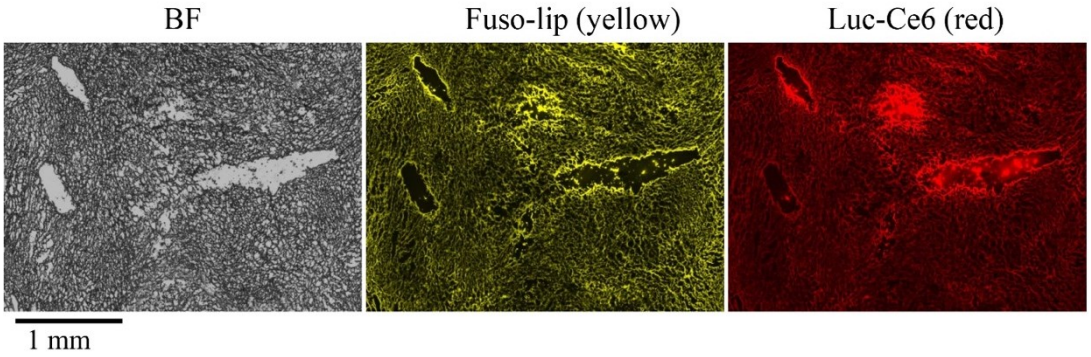

Figure S17. Images of a tumor harvested from the mouse model after BL-PDT *in vivo*, showing the distribution of Luc-Ce6/Fuso-lip around three different injection sites visualized by the needle-induced tissue damage. Similar results were obtained from 3 mice.

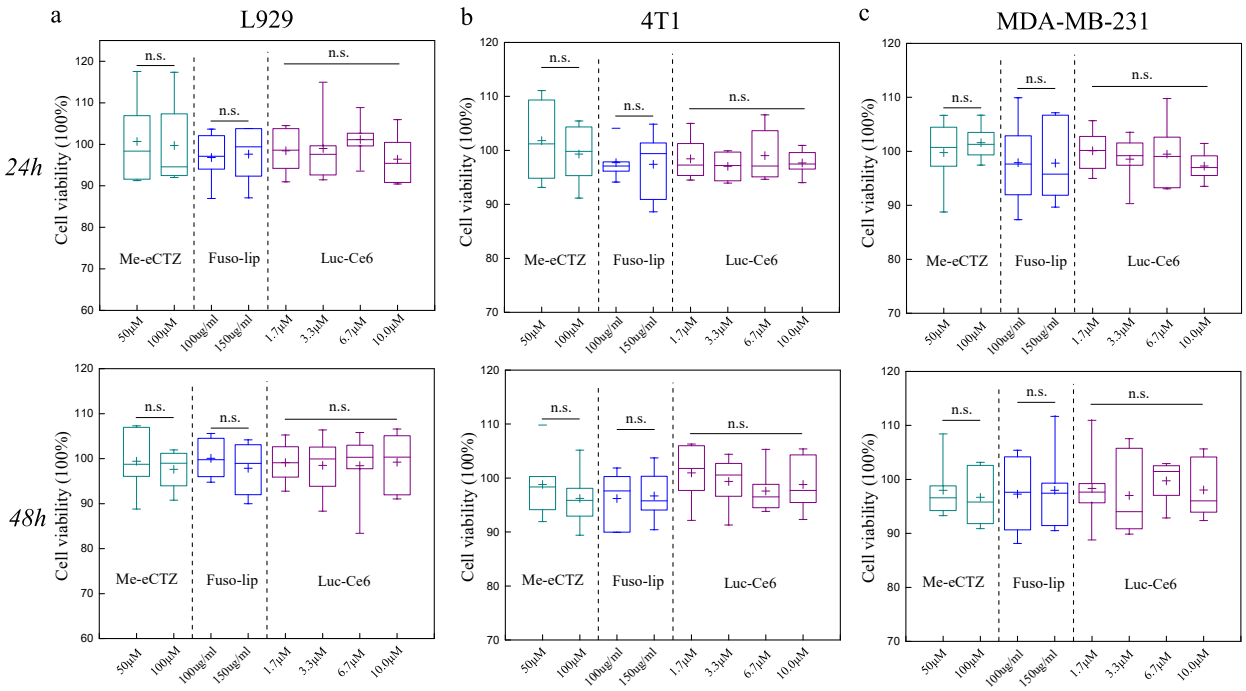

Figure S18. Relative viability of L929 murine fibroblast cells, 4T1 murine triple-negative breast cancer (TNBC) cells, and MDA-MB-231 human TNBC cells after incubation with CTZ, Fuso-lip, and Luc-Ce6/Fuso-lip. The viability was quantified by the ratio of the number of live cells after 24 or 48 hr of incubation to the initial number of cells. In all conditions, no degradation of viability is measured. Values are means ± s.d. (n = 6 wells per group).

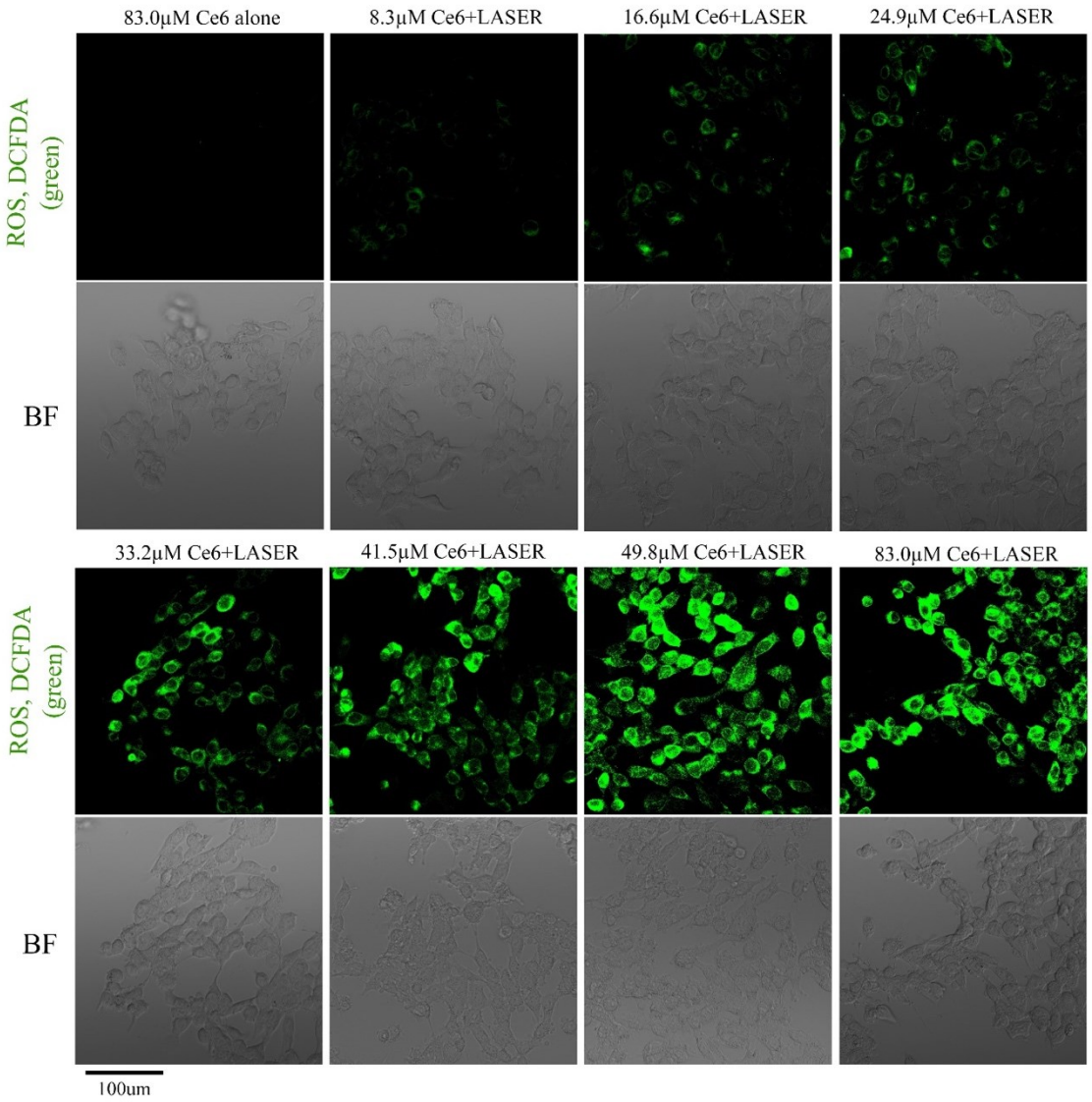

Figure S19. Bright-field (BF) and confocal microscopy images of 4T1 cells after laser-PDT. At the same laser excitation condition (405 nm, 1 J cm^{-2}), the intracellular concentration of ROS is increased with Ce6 concentration.

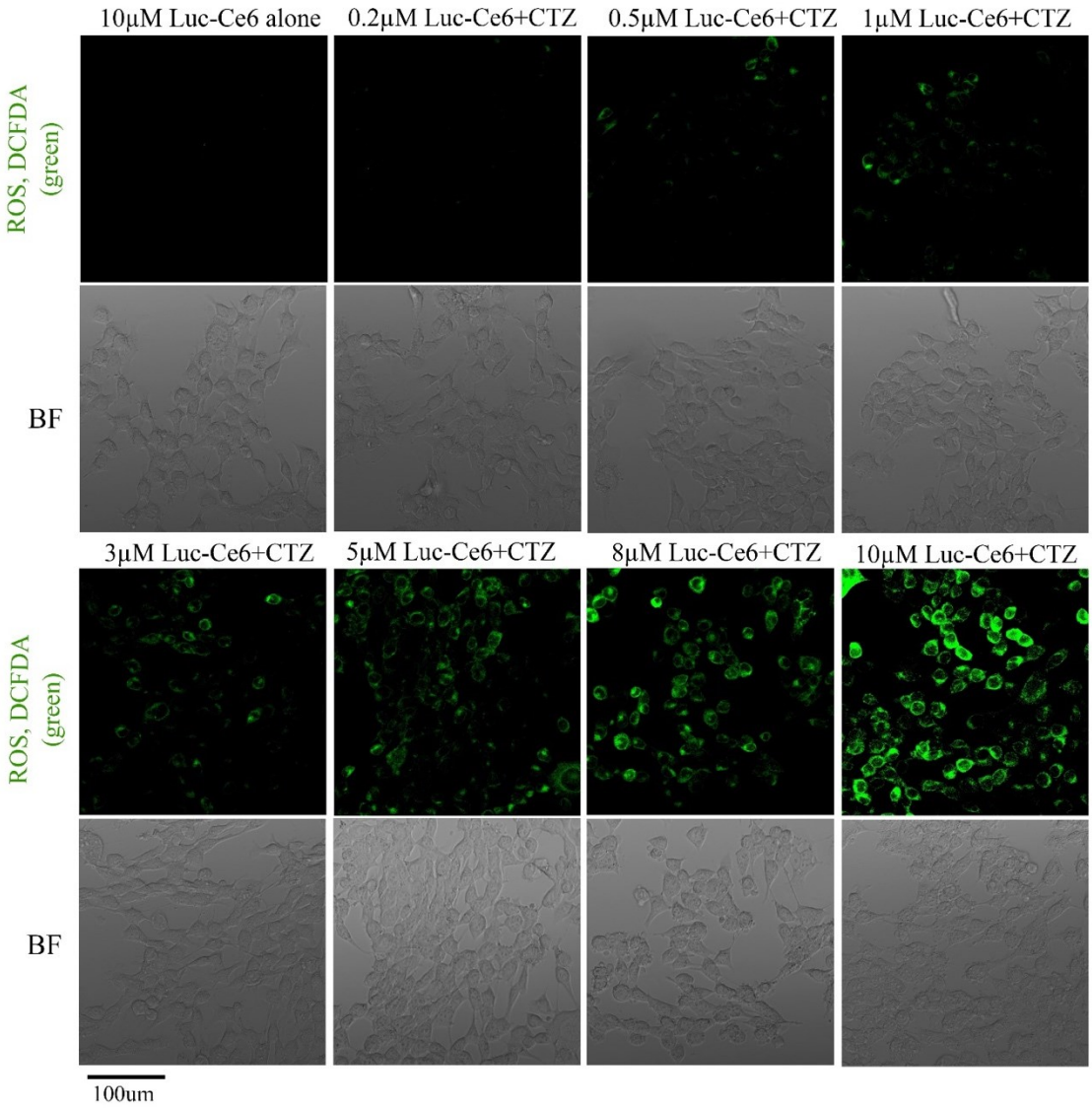

Figure S20. Bright-field (BF) and confocal microscopy images of 4T1 cells after BL-PDT (10 μM Luc-Ce6). For the same CTZ dose (100 μM, 4 hrs.), the intracellular concentration of ROS is increased with Luc-Ce6 concentration.

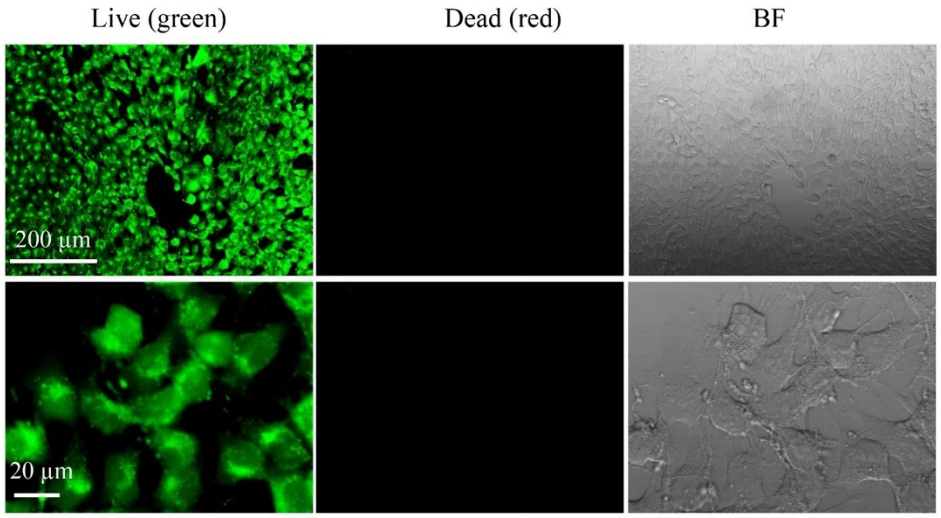

Figure S21. Bright-field (BF) and fluorescence images of non-treated 4T1 cells stained with Calcein AM (live cells, green) and BOBO-3 Iodide (dead cells, red). No dead cells are found in the non-treated group.

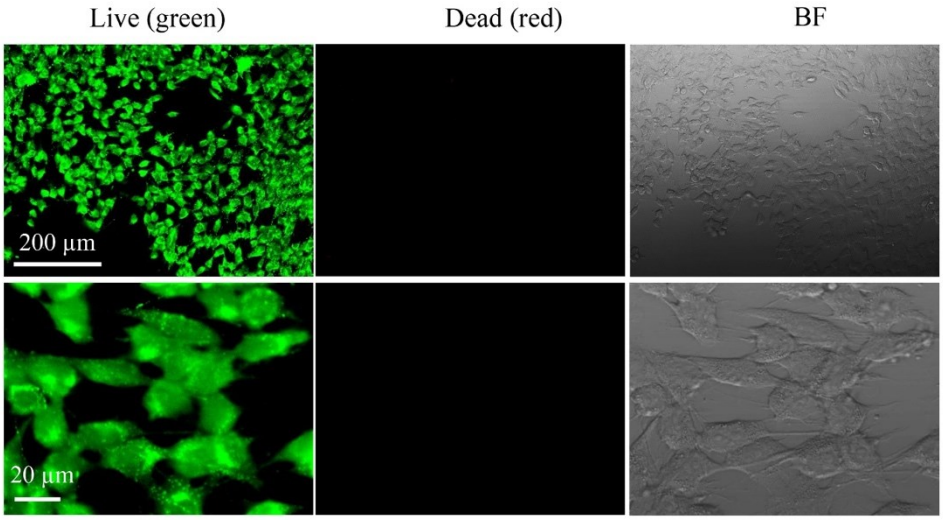

Figure S22. Bright-field (BF) and fluorescence images of 4T1 cells incubated with CTZ (100 µM, 4 hrs. incubation), stained with Calcein AM (live cells, green) and BOBO-3 Iodide (dead cells, red). No dead cells are found.

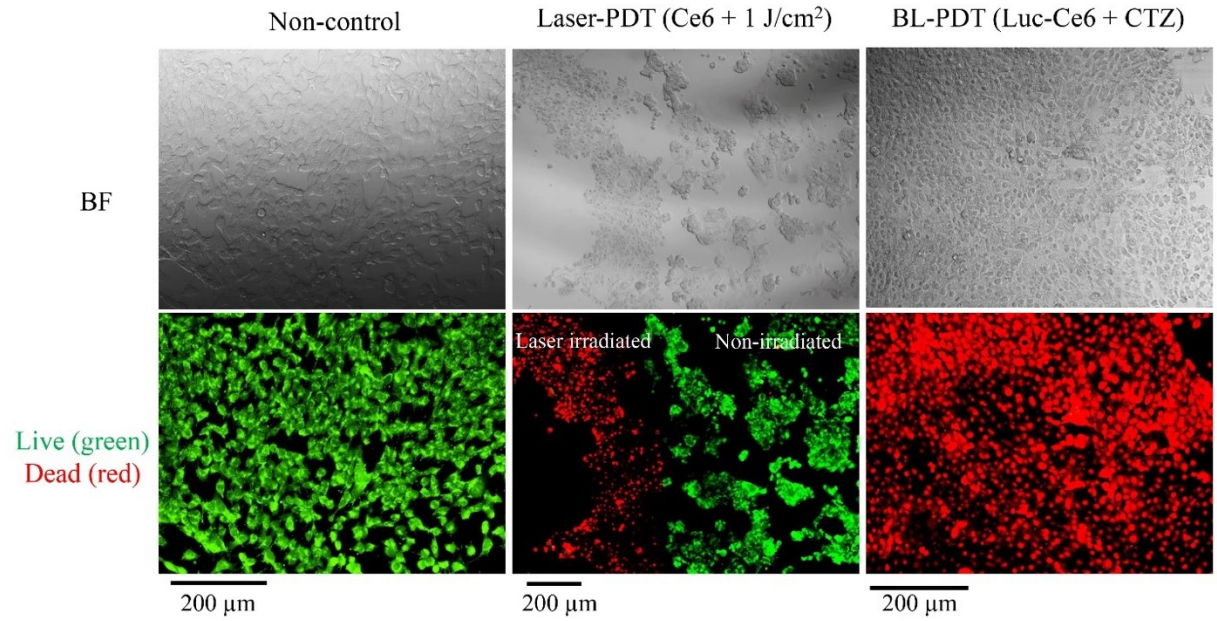

Figure S23. Comparison of 4T1 cells stained with Calcein AM (live cells, green) and BOBO-3 Iodide (dead cells, red), 24 h after treatment. In laser-PDT treated group (41.5 μM Ce6, 405 nm, 1 J cm^{-2}), cell death is observed only in the laser-illuminated region. In BL-PDT treated group (Luc-Ce6, 100 μM CTZ, 4 hrs.), cell death is extensive over the entire cell sample.

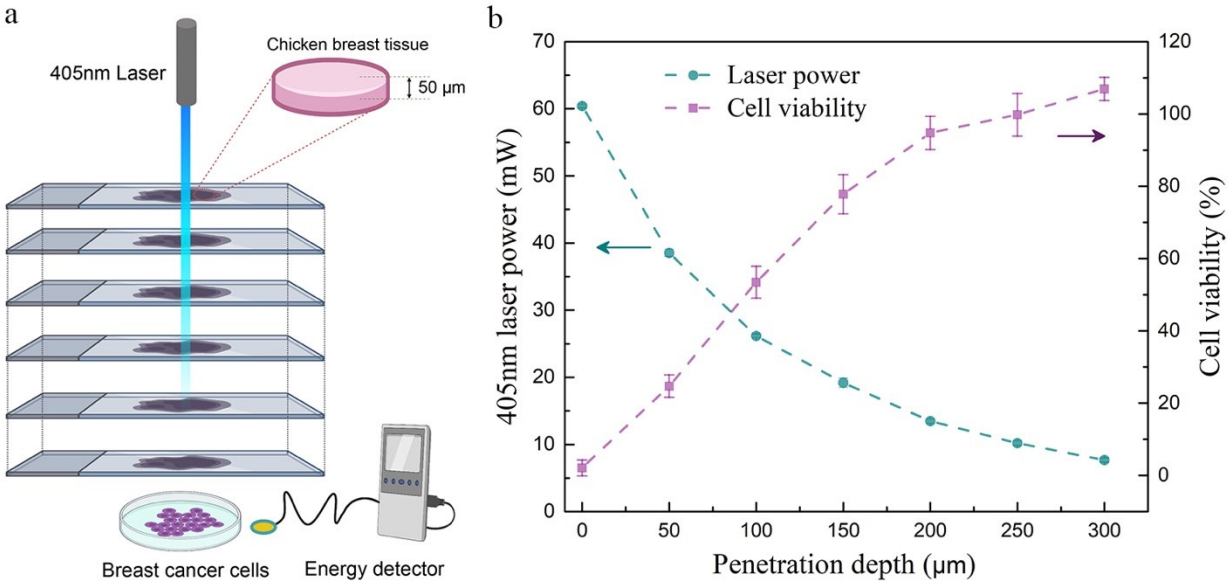

Figure S24. Penetration depth measurement of laser-PDT *in vitro*. (a) Schematic of the setup for illuminating 4T1 cells through chicken breast tissue slices. Each tissue slice is 50 μm in thickness, fully spread on a glass slide. (b) Measured laser power (blue) and cell viability (purple) as a function of the total tissue thickness corresponding to the penetration depth. When the tissue thickness is 300 μm (6 tissue layers), the optical power on the cell sample is reduced to ~ 8 percent of the initial power, and almost no killing of 4T1 cells is observed.

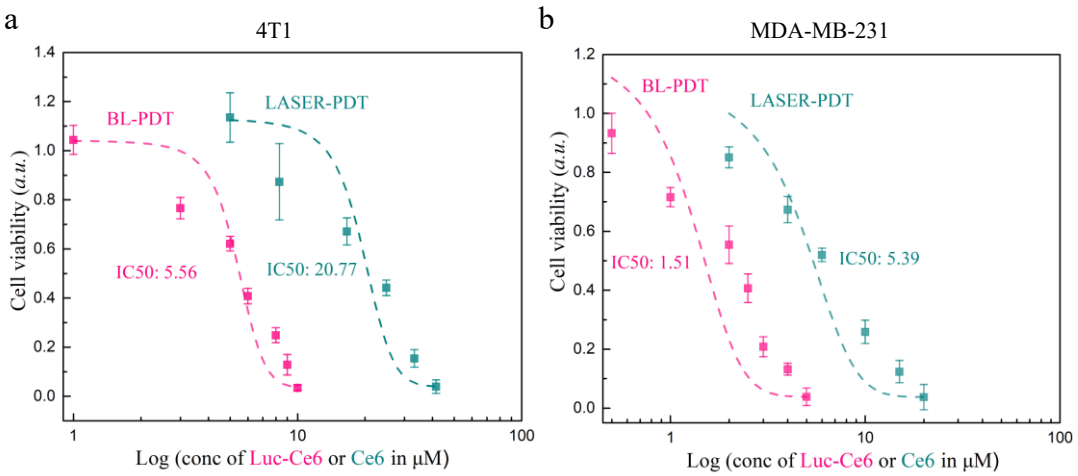

Figure S25. Relative viability of 4T1 cells and MDA-MB-231 cells after laser-PDT (1 J/cm^2) and BL-PDT (100 μM CTZ) for different concentrations of Luc-Ce6 or Ce6. Values are means ± s.d. (n = 5). The dashed lines are fitted curves based on the pharmacologic theory. From the fitting curves, the half-maximal inhibitory concentration (IC_{50}) values are determined. The potency of BL-PDT is 20.77 / (5.56×25) = ~ 0.15 for 4T1 cells and 5.39 / (1.51×25) = ~ 0.14 for MDA-MB-231 cells.

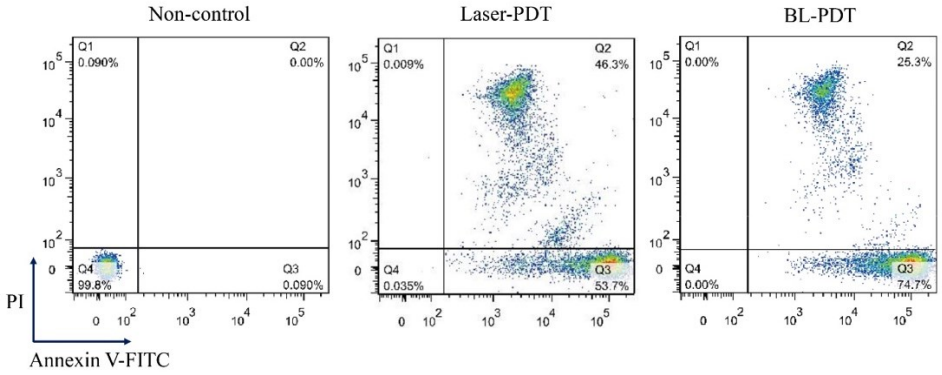

Figure S26. Flow cytometry data of cellular death marker Annexin V-FITC/PI in 4T1 cells 24 hrs. after different treatments. Q1: dead cells, Q2: late apoptosis, Q3: early apoptosis, Q4: live cells. Laser-PDT: 41.5 μM Ce6, 405 nm laser irradiation, 1 J cm^{-2}. BL-PDT: 10 μM Luc-Ce6, 100 μM CTZ for 4 hrs.

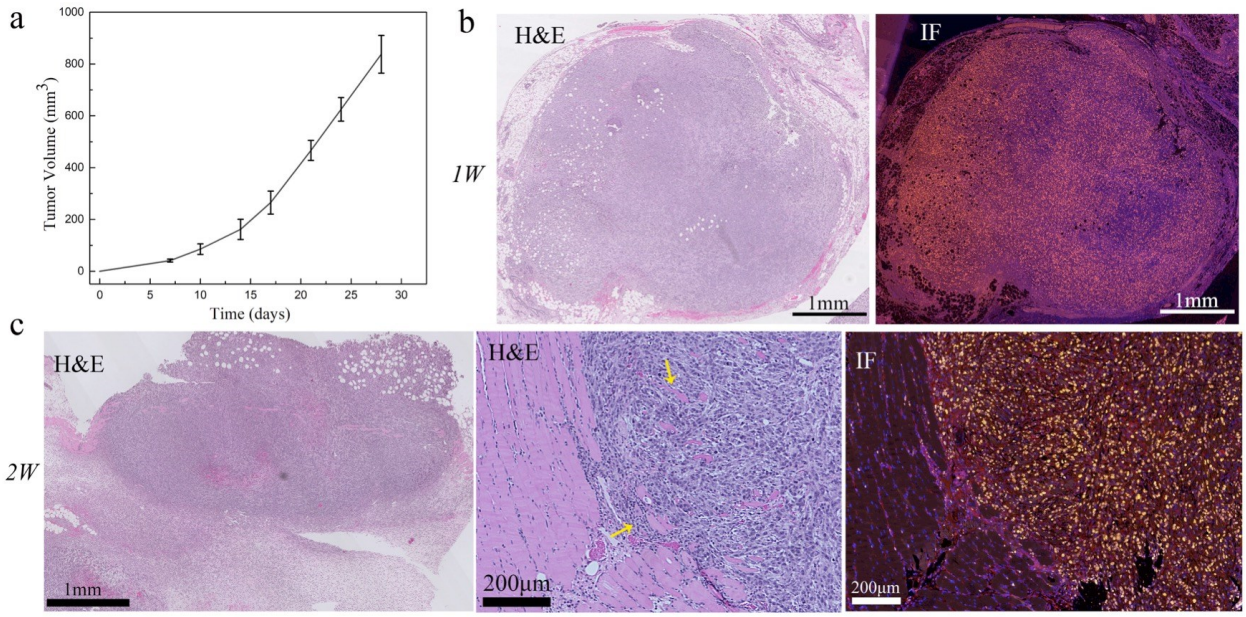

Figure S27. The growth of 4T1 tumor after orthotopic implantation in Balb/c mice. (a) Tumor size variation over time. Error bars indicate ± s.d. (n = 5 mice per group). (b-c) H&E and immunofluorescence (IF) staining of tumor tissues harvested (b) one week or (c) two weeks after implantation. Nuclear marker Ki-67 was labeled with eFluor 570 dye (yellow); cell membrane marker EGFR was labeled with AlexaFluor 647 dye (red), and the nucleus was stained with DAPI (blue). At Week 1, the average tumor size is about 4 mm. At Week 2, the invasion of tumor cells into surrounding tissues (yellow arrows in the middle figure).

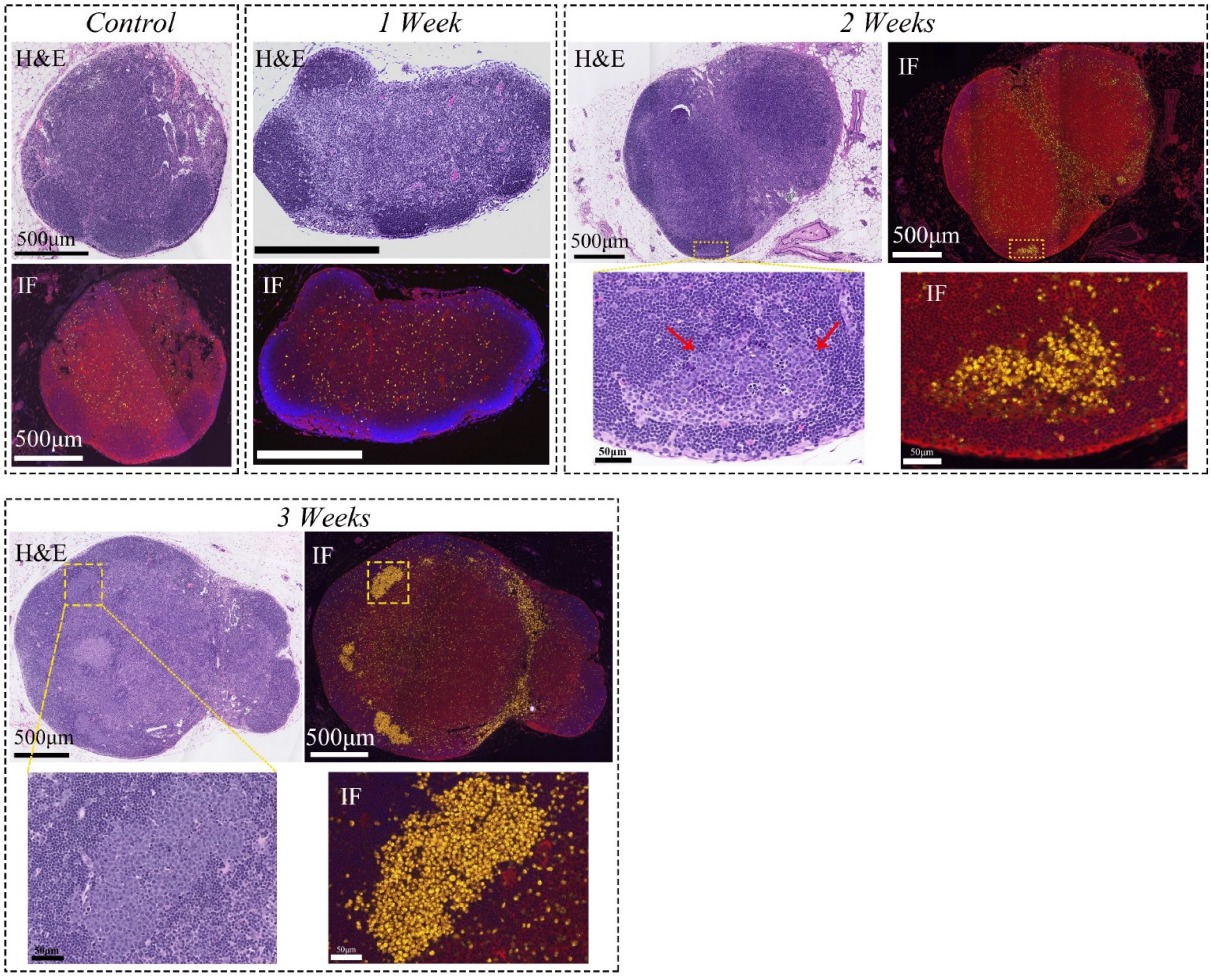

Figure S28. Histological examination of the sentinel lymph nodes in the orthotopic TNBC model. At Week 1 after tumor cell injection, there was no apparent metastasis in the lymph nodes. Nuclear marker Ki-67 was labeled with eFluor 570 dye (yellow); cell membrane marker EGFR was labeled with AlexaFluor 647 dye (red), and the nucleus was stained with DAPI (blue). At Week 2, some small microtumors with sizes of 100 to 200 μm is found in the lymph nodes. At Week 3, extensive metastases are found with sizes of 400 to 500 μm. IF staining: immunofluorescence staining. Similar results were obtained from 3 mice for each time point.

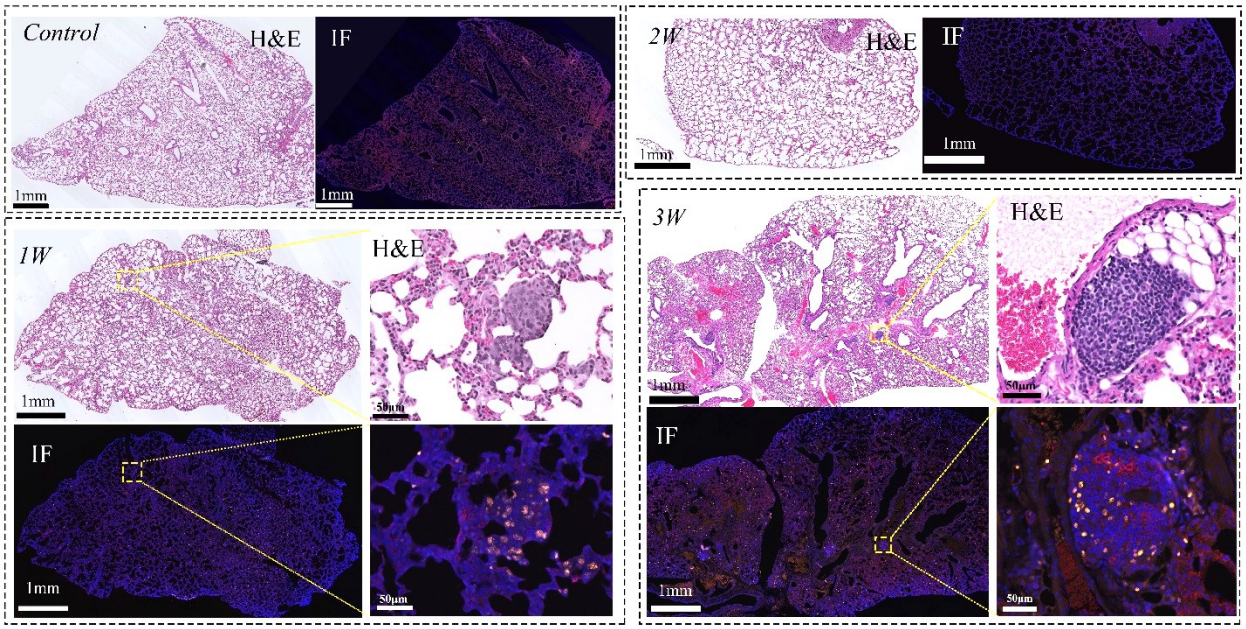

Figure S29. Histological examination of lung tissues harvested from the orthotopic 4T1 TNBC mouse model at different time points: Control (prior to cell inoculation), 1 week, 2 weeks, and 3 weeks post cell inoculation. Ki-67 was labeled with eFluor 570 dye (yellow); EGFR was labeled with AlexaFluor 747 dye (red), and the nucleus was stained with DAPI (blue). At Week 1, no metastasis occurred in the lung. At Week 2, micro-metastases with sizes less than 200 μm are observed. At Week 3, more metastatic foci throughout the lung are evident, with sizes of 250 to 400 μm. IF staining: immunofluorescence staining. Similar results were obtained from 3 mice for each time point.

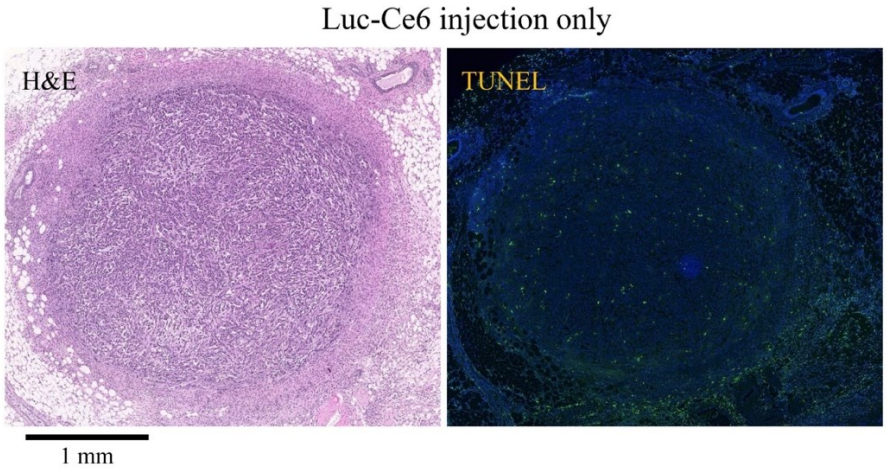

Figure S30. H&E and TUNEL-stained tumor sections harvested 3 days after intra-tumoral injection of Luc-Ce6/Fuso-lip without CTZ. Green: TUNEL signal, apoptotic cells, blue: DAPI, nucleus. No apparent sign of apoptotic cells is found. Similar results were obtained from 3 mice.

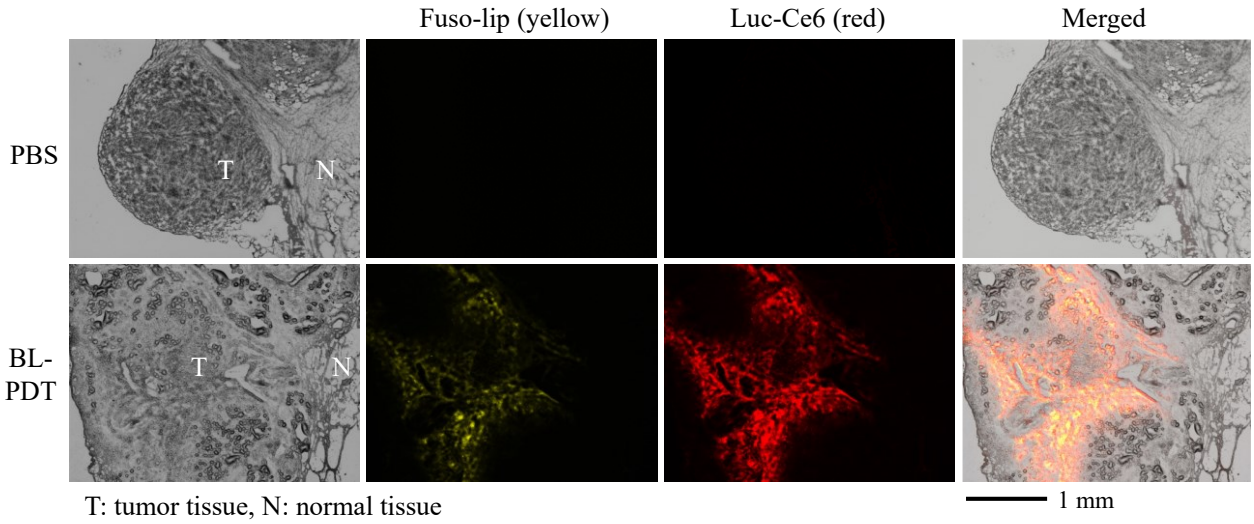

Figure S31. Images of tissue sections obtained from control and BL-PDT treated mice. PBS for the control group and Luc-Ce6/Fuso-lip was injected carefully into the border between tumor tissue (T) and normal tissue (N). Similar results were obtained from 3 mice in each group.

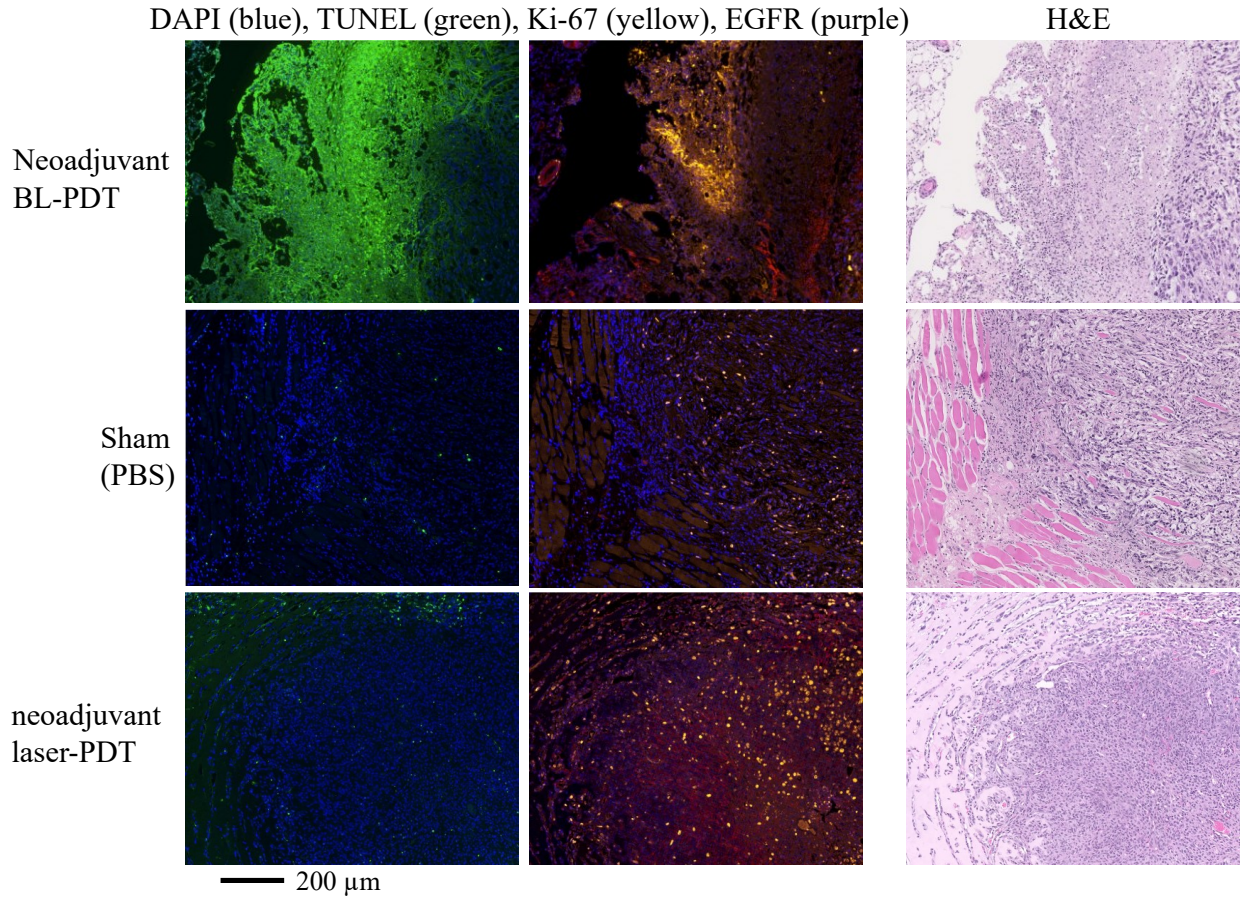

Figure S32. Images of tumor sections obtained 5 days after different treatment. The tumor borders are more clearly visualized after neoadjuvant BL-PDT, owing to the apoptotic death of tumor cells at the boundary. Similar results were obtained from 3 mice in each group.

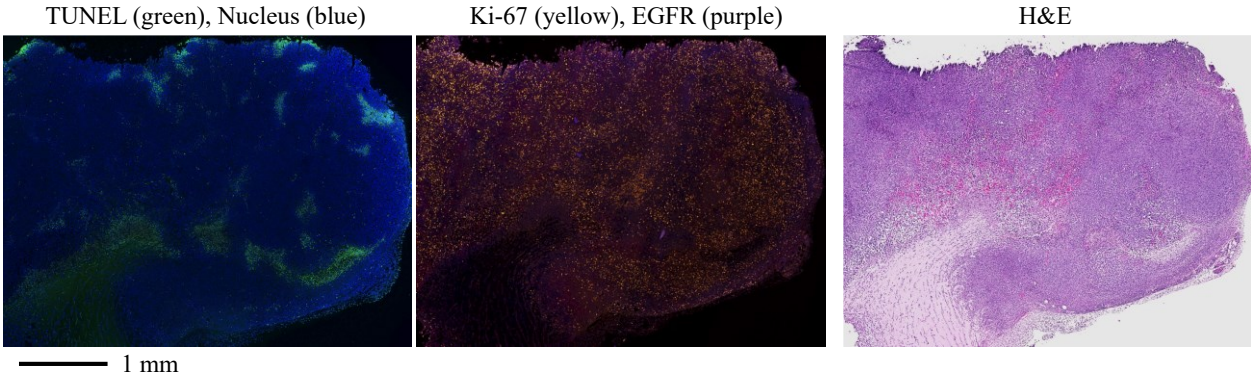

Figure S33. Images of tumor sections obtained 5 days after neoadjuvant laser-PDT (405 nm, 90 J cm^{-2}). No apparent apoptotic tumor cells are found at the tumor boundary. Similar results were obtained from 3 mice.

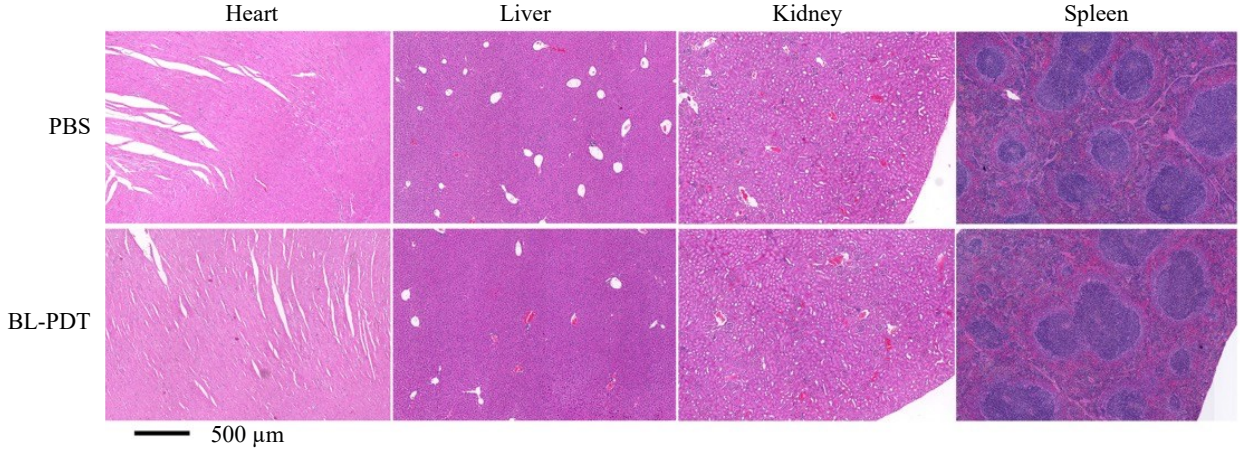

Figure S34. Histological analysis of tissues from several different organs 18 days after PBS injection (top) and BL-PDT (bottom) at 4T1 tumors *in vivo*. No noticeable difference is found between control and treated mice, indicating no apparent side effects of intra-tumoral BL-PDT. for four significant organs. Similar results were obtained from 3 mice in each group.

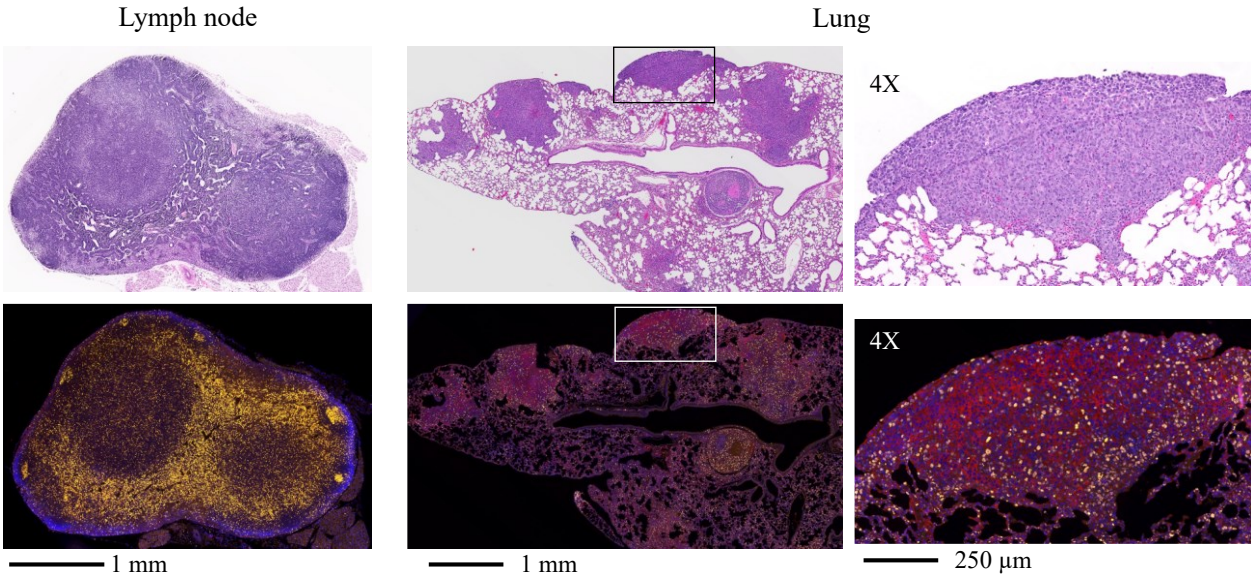

Figure S35. Histological analysis of the sentinel lymph node and lung tissues harvested from tumor-bearing mice 18 days after intra-tumoral injection of Luc-Ce6/Fuso-lip (without CTZ injection). Ki-67 antibody/eFluor 570 (yellow), EGFR antibody/Alexa Fluor 747 (red), and DAPI (blue). Apparent metastasis in the sentinel lymph nodes and lungs were founded from 3 mice.